Volume 14, Issue 3, 142441 (1-23)

Iranian Journal of Catalysis (IJC)

https://doi.org/10.57647/j.ijc.2024.1404.41

Design, synthesis, and characterization of CeO_2 and SnO_2 nanoparticles for enhanced UVA-light-driven photocatalysis

Elaziouti Abdelkader*, Laouedj Nadjia

Laboratoire des Matériaux Inorganiques et Application, Université des Sciences et de la Technologie d'Oran Mohammed Boudiaf (USTO-MB), Oran, Algérie.

Corresponding author: abdelkader.elaziouti@univ-usto.dz

Review Paper

Received:
24 June 2024
Revised:
03 August 2024
Accepted:
10 September 2024
Published online:
08 October 2024

Abstract:

In this study, XRD peak profile investigation was performed on CeO_2-500 and SnO_2-450 materials to assess microstructural parameters. Scherrer (SM, SEAM, and SSM), Monshi-Scherrer (MSM), Williamson-Hall, Size-Strain plot (SSPM), and Halder-Wagner (HWM) models were explored. Additionally, these materials were exploited in heterogeneous photocatalysis experiments. Structural characterization revealed the formation of cubic fluorite type CeO_2 phase and pure tetragonal rutile structure of SnO_2. All methods provide crystallite sizes within $10-12$ nm for CeO_2-500 and $20-30$ nm for SnO_2-450. SSPM gave the highest values of intrinsic strain and R^2 (0.9975) along with satisfactory crystallite size, while the HWM model provided the highest R^2 and exhibited a decrease in the intrinsic strain, which would suggest that lattice ε was isotropic in the environment. SEM analysis showed spherical NPs of CeO_2-500 and consisted of a foamed body of SnO_2-450. Both materials are legitimately transparent in the entire UV-Vis region with optical gap energy of 3.1 eV for CeO_2-500 and 3.35 eV for SnO_2-450. Ultimately, both materials exhibited excellent performance as a result of 76.44 and 61.63% degradation achieved under UVA-light illumination for CeO_2-500 and SnO_2-450, respectively. Consequently, the outstanding degradation of CR could be can be synergistically explained by the photocatalysis oxidation procedure mechanisms through ROS (•OH, $O_2^{\bullet-}$) as the robust oxidizing agents implicated in oxidation and reduction processes with large intrinsic crystal defects (Ce^{4+}-O and Sn^{4+}-O defects sites) as primary driving forces ultimately facilitate charge separation of carriers, reduce their recombination rate and thus boost their photocatalytic effectiveness.

Keywords: CeO_2; SnO_2; XRD peak profile analysis; Congo red (CR); Degradation; Kinetics; Photocatalysis; Synergy

1. Introduction

Nanoscience and nanotechnology are considered the fundamental high-tech aspects of the 21^{st} century [1, 2]. CeO_2 NPs, as rare earth metal oxide (REMO), and SnO_2 NPs, as transparent conducting oxide (TCO), were considered as promising candidates in energy, environment, and biological applications. Among a myriad amount of nanoparticles, such as CeO_2 (cerium dioxide), as an important inorganic rare earth metal oxide (REMO), has been attracting great interest in the past decade due to its widespread variety of energy, environment, and biology-related applications. CeO_2 has been considered a key material and was extensively used owing to its wide range of applications in solid-state electrolytes for electrochemical devices [3], catalysts for three-way automobile exhaust systems (TWC) cycling between reduced and oxidized states ($Ce^{3+} \leftrightarrow Ce^{4+}$) [4], polishing agents for chemical-mechanical planarization process [5], and ultraviolet (UV) blocking materials in UV shielding [6], the adsorption and reaction of formaldehyde [7], oxygen storage capacity [8], hybrid solar cells [9], H_2S removal [10], luminescent materials for violet/blue fluores-

cence [11] as well as antioxidants in biotechnology and medicine [12–14]. Transparent conducting oxides (TCOs) such as ZnO, In_2O_3, and SnO_2 NPs have been attracting a great deal of research interest owing to their outstanding optical, electrical, and magnetic properties of semiconducting nanoparticles. These intriguing properties make SnO_2 a promising candidate for basic research and technological applications alike. These uses depend on the inherent physicochemical properties of nanoscale materials and the specific ability of CNPs to uptake and release oxygen [15–19], dye-sensitized solar cells [20], field emission displays [21], luminescent devices [22], photovoltaic solar energy conversion [23, 24], transparent electrodes [25], transparent conducting films [26], catalytic materials [27], environmental monitoring [28], biochemical/chemical sensor [29, 30], lithium batteries [31]. This oxide with the band gap energy close to visible light [32, 33] has been investigated in photocatalytic and electro-catalytic processes [34–37]. CeO_2 crystallizes in a cubic crystal structure and in its unit lattice; each Ce^{4+} cation is coordinated by 8 O_2^- anions. The empty 4f orbital and abundant electronic energy stages make CeO_2 as a good condidate in catalysis. The Ce^{3+}/Ce^{4+} redox couple offers the possibility to generate strong interactions with other components in catalysts and thereby boost the functioning of electrocatalysts as well as photocatalysts. The multivalence property of CeO_2 will offer the opportunity to generate strong interactions with other components in catalysts and thereby enhance the performance of electrocatalysts and photocatalysts. CeO_2 NPs is associated with rich oxygen vacancies, Ce^{3+} defects present in CeO_{2-x} and the relative thermodynamic efficiency of redox cycling between CeO_2 and Ce_2O_3 (Ce^{3+}/Ce^{4+}) under oxidizing and reducing conditions, therefore promoted as a higher capacity oxygen storage material [38, 39]. Loss of oxygen and/or its electrons forms oxygen vacancies or defects in the lattice. This defect results in lattice strain in crystals. The distortion may arise and change with temperature, oxygen partial pressure, doping with other ions, electrical field, or surface stress. Under lean fuel conditions, CeO_{2-x} adsorbs oxygen in the forms of $O_2^{\bullet-}$ and O_2^{2-}. Under rich fuel conditions, the stored oxygen in CeO_2 is released with regeneration of CeO_{2-x}. In CeO_2 NPs, non-stoichiometric oxygen atoms are present at the grain boundary, and these vacancies play an important role in the stable grain boundary structure of CeO_2 NPs [40]. The main concern of CeO_2-based materials is their synthesis routes. Hence, the sizes of the prepared ceria particles are relatively large with the broadband gap energy ($\approx 2.6-3.4$ eV) [41] and relatively high dielectric constant value ($\varepsilon = 23-52$) [42]. On the other hand, the naturally occurring form of stannic oxide (SnO_2) is the mineral cassiterite. SnO_2 has a different sequence of polymorphs such as rutile-type (tetragonal), $CaCl_2$-type (orthorhombic; Pnnm), α-PbO_2 (orthorhombic; Pbcn), pyrite-type (cubic; Pa-3), ZrO_2-type(orthorhombic; Pbca) and cotunnite-type (orthorhombic; Pnma) structures. SnO_2 polymorphs undergo sequential phase transitions with the change in pressure [43] by heating or by having both strategies at the same time. It adopts the rutile structure with a tetragonal unit cell. The structure of SnO consists of chains of SnO octahedra in which each Sn atom is octahedral, surrounded by six oxygen atoms, while each oxygen is surrounded by three Sn atoms arranged at the corners of an equilateral triangle. The structure's Sn:O coordination is 6:3, with each octahedron not being regular, showing a slight orthorhombic distortion. SnO_2 possesses a versatile large band gap (3.6 eV at 300 K), a melting point of 1127 °C, and a density of 6.95 g.cm^{-3} at room temperature. Fascinatingly, the simultaneous occurrence of transparency and conductivity of SnO_2 is a unique feature among the Group-IV elements of the periodic table. SnO_2 NPs is considered as a very suitable material for the electron transport layer application because of its properties namely, chemical stability, optical transparency, low resistivity and piezoelectric behavior, high exciton binding energy of 130 meV. Due to the larger band gap and high achievable carrier concentration (up to 6x 1020 cm^{-3}), SnO_2 exhibits oxygen vacancy, higher carrier density, and outstanding electrical and optical properties. The diversitability of the applications is found to be a function of the size, morphology, phase, and crystallinity of the nanocrystal. Nowadays, advanced oxidation processes (AOPs) as a promising wastewater treatment technique have been intensively focused on by researchers/scientists over various other conventional techniques. In comparison, the utilization of advanced oxidation processes such as ultrasonic/microwave-assisted degradation, ozonation, non-thermal, photocatalysis, Fenton/photo-Fenton, sonolysis, and the electrochemical process can achieve higher degradation activity towards refractory organic pollutants. In contrast, heterogeneous photocatalysis progressively and thoroughly degrades toxic contaminants through the generation of free radicals (•OH), as a highly reactive species, depicting the pros of green, efficient, and low-cost technology than others [44]. Semiconducting-based photocatalysis is an efficient tools that has been extensively exploded for the decomposition of hazardous organic and inorganic compounds. In this heterogeneous process concept, when a semiconducting material is stimulated by sufficient photon energy (energy of photons should be equal to or greater than the energy gap (Eg) of the semiconductor), commonly in the UV and visible regions of the light, the electrons (e-) and holes (h^+) pairs can be easily separated and directly participated in the degradation of the subjected pollutant via reduction and oxidation processes, respectively. In the reduction process, photogenerated electrons (e-) can reduce the dissolved oxygen (O_2) to yield the superoxide radicals ($O_2^{\bullet-}$), as robust reactive species. In contrast, the photoinduced holes (h^+) can react with either the water molecules (H_2O) or hydroxyl anions (OH^-) to produce hydroxyl radicals (•OH) as powerful oxidizing agents. These reactive oxygen species ROS (•OH and $O_2^{\bullet-}$) can effectively undergo reaction with the pollutants to form intermediate products and finally mineralize to H_2O and CO_2. The overall effects of all the processes highlighted above are function of the two foremost factors (i) REMOs and TCOs materials band gap energy and (ii) materials band bending phenomenon. Unfortunately, the photoinduced electrons (e-) and holes (h^+) pairs may recombine and severely reduce the overall efficiency of a typical photodegradation process [45].

Because of their intrinsic characteristics, wider band gaps, multivalence behaviors, high refractive index, high optical transparency in the visible region, specific surface defects (abundant oxygen vacancies and large surface area), outstanding thermal and chemical stability, good catalytic activity, high thermal stability and multifunctional design, CeO_2 and SnO_2 being considered as a photoelectrode and magnetoelectric material applicants respectively as well as the most efficient photocatalysts to degrade organic and /or inorganic pollutants under the UV wavelength region (absorption edge up 400 nm) [46–54]. Despite these unique performances, major challenges that are currently faced by both materials which limit their further applications are large band gap ($\approx 2.6-3.6$ eV), soft valence band (VB) and soft conduction band (CB) positions, poor light absorption, small surface area and serious recombination of photoinduced charge carriers which is inevitable for traditional CeO_{2-} and SnO_{2-} based photocatalysts under visible or solar wavelength regions. Consequently, the photoinduced electrons (e-) and holes (h^+) pairs may promptly recombine due to the strong Coulombic force between electron and hole, and severely reduce the overall efficiency of typical photocatalytic and photoelectrocatalytic degradation processes. So, to prevent these above shortcomings, numerous modification techniques of CeO_2 and SnO_2 have been utilized to enhance the capability of light harvesting these materials to the visible light region and boost their optoelectric, electrophotelectric, and photocatalytic performances such as changes in morphology, adding support materials, doping metals and non-metals, and fabricating heterojunctions semiconductor through various synthetic strategies including sonochemical synthesis [55] microwave-assisted hydrothermal [56], homogeneous precipitation technique [57], sol-gel [58] and microwave-assisted solvothermal methods [59], green synthesis, thermal vapor deposition (TVP) and chemical vapour deposition (CVD) [59–63], microwave oven [64] co-precipitation [65] and solid-state [66]. Despite the enormous advancement in these synthetic approaches, the intrinsic performances of single CeO_2 and SnO_2 reaction mechanisms are still controversial and unsettled. Additionally, the above-mentioned techniques strongly alter CeO_2 and SnO_2 crystallographic parameters (lattice symmetry, cell parameters, and microstructural properties) with high surface energy and are unstable phases in a bulk form. Therefore, further investigations and horizon are immediately needed to synthesize CeO_{2-} and SnO_{2-} based catalysts with unique performances and outstanding efficiencies in the opto-, photo- and photoelectrodegradation processes utilizing visible light or even solar energies.

It is recognized that the broadening in the XRD peaks are the most reponssible effects for occurrence of size confinement and intrinsic strain in nanocrystals [67] caused by crystallographic defects [68]. Numerous methods such as XRD, SEM, TEM, EDS and BET, etc. were used for determining the crystal size of nanomaterials.

Nonetheless, by using XRD peak widening analysis, the microstructure parameters can be easily assessed. There are various methods, such as the Scherrer model, which predicts the size of crystallites based on the full width at half maximum (FWHM=βhkl) of the prominent reflection peak. Meanwhile, the Scherrer equation average method (SEAM) was used to calculate the crystallite size for all the selected βhkl individually and obtain the average. In the Sahadat-Scherrer Model (SSM), the straight line should go across the origin. In the SSP method, both Lorentzian (function considers size broadening) and Gaussian (function considers strain broadening) are integrated in this model. The Halder-Wagner (H-W) method assumes that the spreading of the peak is a symmetric Voigt function, which means that the crystallite size is defined by the Lorentzian and Gaussian functions [69]. The Williamson-Hall (W-H) analysis is a simplified integral breadth method where both size-induced and strain-induced broadening are deconvoluted by considering the peak width as a function of 2θ. Williamson-Hall method uses the FWHM of the diffraction peak, and hence, it is a very easy and more realistic suitable one for determination of the average crystallite size and microstrain. Meanwhile, the Voigt function is considered for peak broadening as per the Halder-Wagner method. The results obtained from the SSP and H-W methods prove to be more accurate than the Williamson-Hall method as low and middle-angle diffraction data are taken into account. Among these models, the Williamson-Hall model also comprises three other models : the uniform deformation model (UDM), the strain in the uniform deformation stress model (USDM), and the uniform deformation energy density model (UDEDM), that takes into account the anisotropic nature of Young's modulus of the crystal and are used to measure microstructure parameters. The Monshi Scherrer method (MSM) provides a more accurate value of the average crystallite size from all or some of the different peaks. In our present research, we report the design and synthesis of CeO_2 and SnO_2 NPs via homogeneous precipitation methods and calcined at 500 °C (i.e., CeO_2-500) and 450 °C (i.e., SnO_2-450) and subsequently identified by XRD, SEM and UV-vis-RD technique. This study endows a forceful approach to design and develop REMO and TCO materials with unique morphological, electronic and optical structures for photocatalytic reactions. Additionally, the XRD peak profile analysis was performed to determine various microstructural parameters, i.e., crystallite size, lattice parameters, dislocation density, intrinsic strain, Young's modulus, stress, and anisotropic energy density. Further, the photocatalytic achievements of CeO_2 and SnO_2 NPs were assessed with regard to the photocatalytic degradation of Congo red (CR) azodye as prototypical contaminants when exposed to UVA-light irradiation. Five preliminary experiments: UVA-lights alone (CR /UVA process), CeO_2 and SnO_2 catalysts alone (CR/CeO_2 and CR/ SnO_2 systems), and CeO_2 and SnO_2 in the presence of UVA-light (CR /CeO_2/UVA and CR /SnO_2/UVA processes) were explored. The photodegradation reactions were correlated with the pseudo-first-order kinetic model. Possible photodegradation mechanisms pathways were highlighted in detail.

2. Experimental

2.1 Reagents used

All the chemicals used in this study were of analytical grade without further purification. Cerium (III) nitrate hexahydrates ($Ce(NO_3)_3.6H_2O$; 99.99%), tin dichloride dihydrate ($SnCl_2$.$2H_2O$; 98 wt%), and oxalic acid dihydrate ($H_2C_2O_4$; 99.5 wt%) were provided from Aldrich chemical company ltd. Ethylene glycols ($C_2H_6O_2$), Congo red (CR) azodye, Ammonium hydroxide solution ($NH_4OH \geq 99.0\%$) and Sulfuric acid ($H_2SO_4 \geq 99.0\%$) were purchased from I.S.A Espagne. Table 1 depicts CR dye azodye 3 D molecular structure and its related chemicals and physical properties.

2.2 Synthesis of cerium oxide

In a regular trial, 80 mL of ethylene glycol ($C_2H_6O_2$) was dissolved in 20 mL of deionized water. Then, 10.91 g of cerium (III) nitrate hexahydrates ($Ce(NO_3)_3.6H_2O$) was added to the above solution under stirring and at $60-70$ °C for 1 hour. Afterwath, 25 mL of ammonium hydroxide (NH_4OH) solution at 3.0 M was dropwise added to, the reactant solution up to pH $>$ 9. The synthesized solution was maintained at $60-70$ °C for a further 24h. Ultimately, the precipitate was collected by centrifugation (3500 rpm for 15 min) and then washed three times with deionized water and ethanol. The precipitate sample was dried overnight. After that, it was powdered and calcined for 2h at 500 °C. It was labeled as CeO_2-500.

2.3 Synthesis of tin oxide

A known amount of tin dichloride dihydrate was added to a 250 ml 0.4 M solution of $SnCl_2.2H_2O$ and magnetically stirred at room temperature for 1 hour. A stoichiometric amount of $H_2C_2O_4$, as a chelating agent, was progressively added to the above solution ($SnCl_2.2H_2O$ and $H_2C_2O_4$ were mixed in a molar ratio of 1:1). The mixture was then withdrawn and maintained at room temperature for a further 4 hours. After washing with deionized water and ethanol, the mixture was centrifuged, filtered, and finally collected. The obtained precipitate was dried in a hot air oven for 24 hours. After that, it was powdered and calcined at 450 °C for 4 hours and labeled as SnO_2-450.

2.4 Characterization

Bruker D8 Advance XRD diffractometer (Cu-K_α radiation = 0.154178 nm, 2θ=10°-80° and a scanning rate of $10°.min^{-1}$) was used to identify the crystal structures of the studied materials. The morphology of these materials was examined by S4800 Field Emission SEM (FESEM. Hitachi, Japan) Scanning Electron Microscope (SEM). UV–vis-RD spectrophotometer (Perckin Elmer Lambda 920 was utilized to determine the UV–vis diffuse reflection spectra.

2.5 Quantum chemical computation

Geometry optimization of CR molecule and quantum chemical calculations were carried out in the Gaussian-09 revision –D01-SMP program using DFT at B3LYP/6-31G* level of theory. Some theoretical parameters such as E_{HOMO}, E_{LUMO} Eg, η, μ, and ω were reported in the literature [70]. The theoretical reactivity parameters are represented in equations Eq.(1-4SI). The UVA-irradiation and semiconductor band gap energies (Ehν) and (Eg), respectively, can be computed by Planck's Law Eq.(5SI).

2.6 Photocatalytic study

In a typical assay, a known amount of CeO_2 (or SnO_2) catalyst and 200 mL of CR dye solution at 20 $mg.L^{-1}$ were mixed together into a flask with constant agitation and previously adjusted at pH=7 (for CeO_2 experiment) an 8 (for SnO_2 test). The blend was stirred at 25 °C for 1 hour in dark conditions to reach an adsorption-desorption equilibrium. The photocatalytic reaction was undertaken with a 6 W ultraviolet (365 nm, BLX-E365) photoreactor with optimal photon intensity (I = 90 $J.cm^{-2}$) as a UVA-light irradiation source under continuous mixing. The supernatant of the solution (5 mL) was taken from the experiment flask, filtered, and constantly monitored using Analyticjena UV-vis spectrophotometer. The adsorption and photodegradation percentage (%) of both catalysts were obtained from the following equations: Eq.(6SI) and Eq.(7SI).

3. Results and discussions

3.1 Crystallinity analysis

The XRD patterns of CeO_2-500 and SnO_2-450 in the 2θ range from 20 to 80° a long with ICDD standard data are depicted in Figs. 1 and 2, respectively. All XRD peaks of CeO_2-500 observed in Fig. 1 could be indexed to (111), (200), (220), (311), (222), (400), (331), and (420) crystal

Table 1. 3D molecular structure, physical and physical properties of Congo red (CR) azodye (Figure was created using CrystalMaker software).

3D Molecular structure	Chemicals and physical properties
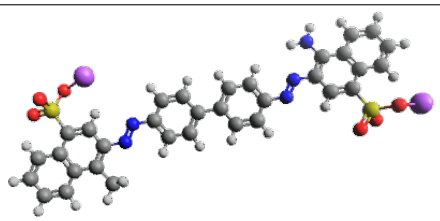	Molecular formula: $C_{32}H_{22}N_6Na_2O_6S_{26}$ λ_{max} (nm): 520 Molar mass (g/moL): 696.665 Melting point (°C): 360 Ebullition pressure (mmHg): 760 Color: Blue(<pH= 4) to Red (>pH=4) Solubility in water (g/L) @25 °C: 25

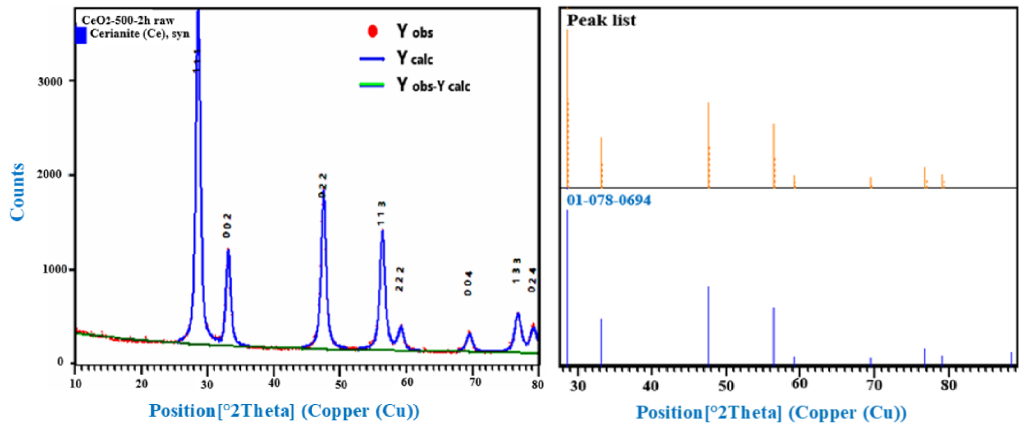

Figure 1. XRD patterns of CeO_2-500 (a) a long with ICDD standard (ICDD File No: 01-078-0694) CeO_2 (cerianite) (b). The observed intensities are shown as red dots, calculated by a solid black and blue line, and the background by a green line.

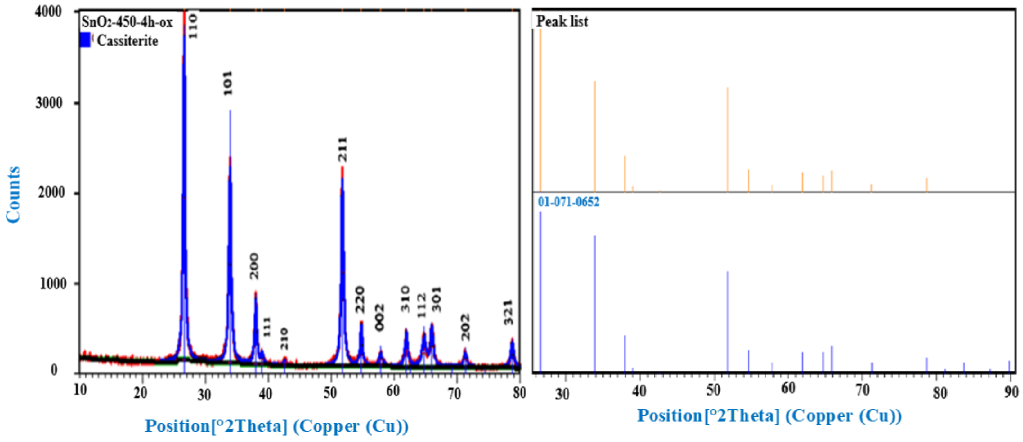

Figure 2. XRD patterns of tin SnO_2-450 (a) along with ICDD standard (File No.01-071-0652) SnO_2 (Cassiterite) (b). The observed intensities are shown as red dots, calculated by a solid blue line, and the background by a black line.

planes cubic fluorite type CeO_2 phase, as per identified reference data ICDD card no: 01-078-0694 of cerium oxide (ceriantite) [71]. On the other hand, SnO_2-450, Fig. 2 exhibited only the tetragonal phase, which well matches with an excellent agreement with the reference data ICDD card no. 01-071-0652 of stannic oxide (Cassiterite) [72], as displayed in Table 2. The major XRD peaks appeared at 2θ of 26.63°, 33.73°, 37.94°, and 51.79° corresponding to the miller planes (110), (101), (200), and (211) of tetragonal rutile-like SnO_2 with space group Fm-3m. The maximum intensity is observed at 2θ = 26.63°, 33.73°, which corresponds to the (110) and (101) miller planes, indicating narrow grain size distribution and high purity [73]. The Bragg's law is given by the following equation

Table 2. Crystallographic parameters of CeO_2-500 and SnO_2-450 materials.

S.I.	Lattice Parameters a (Å) c (Å) α(°) β(°) γ(°)	Volume of Unit Cell, V $(Å)^3$	Crystal density, d (g/cm^3)
ICDD card No: 01-078-0694 CeO_2 (ceranite)	5.411 - 90 90 90	158.428 (2)	7.21
CeO_2-500 NPs	5.4094 - 90 90 90	158.29	7.22
ICDC filcard no.01-071-0652 SnO_2 (Cassiterite)	4.7373 3.1865 90 90 90	-	-
SnO_2-450 NPs	4.743(2) 3.189 (2) 90 90 90	71.75	6.98

S.I : Sample identification

Eq.(8SI). Generally, d_{hkl}-spacing is presented by Eq.(9SI) and Eq.(10SI) for cubic and tetragonal crystals, correspondingly. By using these equations, the lattice parameters (a and c) for both cubic and tetragonal phases were estimated (Table 2).

3.2 Calculation of crystallographic parameters

The volume of unit cells are given by Eq.(11SI) [74] and Eq.(12SI) [75] for cubic and tetragonal crystals, respectively. The crystal density can be computed by Eq.(13SI) [76]. Bearing in mind the primitive cell of a cubic lattice of CeO_2 containing 4 atoms of Ce, whereas that of the tetragonal lattice with an effective number of formula units covering 2 atoms of Sn, the above expression can be transformed as Eq.(14SI) and Eq.(15SI). The local strain in the crystalline materials can be estimated by the following equation: Eq.(16SI). The dislocation density δ (nm^{-2}) was expressed as follows: Eq.(17SI) [77]. The specific surface area (SSA), presuming that both crystals (CeO_2-500 and SnO_2-450 NPs) have spherical shapes and uniform sizes, could be expressed as follows Eq.(18SI) [78].The number of unit cells (n) of CeO_2-500 and SnO_2-450 crystals were calculated using the following formula Eq.(19SI) [79]. The crystallographic parameters of experimental and ICDD data values for CeO_2-500 and SnO_2-450 NPs were tabulated in Table 2.

3.3 Scherrer method (SM)

Scherrer method is used for the determination of the size of crystals in the form of monodisperse powder. The corrected computed broadening (β_{hkl}) of XRD diffractograms in NPs crystals is a function of physical broadening (β_m) and instrumental broadening (β_i). The broadening (β_{hkl}) can be written as Eq. (20SI) [80]. The average crystallite size can be calculated as follows: Eq.(21SI) [81].
By taking β_{hkl} of the broadening of the *hkl*= 111 and *hkl*= 110, as prominent reflection peaks for CeO_2-500 and SnO_2-450, respectively, the estimated DXRD of CeO_2-500 and SnO_2-450 were 10.06 [82] and 22.97 nm [83], respectively, as displayed in Tables 3 and 4.

3.4 Scherrer equation average method (SEAM)

Scherrer average method was applied to measure crystallite sizes for all selected β_{hkl} in the X-ray diffraction pattern (Figs. 1 and 2) individually from Eq.(21SI) and achieving the average. The deduced values of crystallite size for CeO_2-500 and SnO_2-450 and their corresponding averages were displayed in Tables 3 and 4. The average crystallite size DXRD was around 8.75 nm for CeO_2-500 and 18.46 nm for SnO_2-450.

3.5 Linear straight-line method (LSLM)

The linear straight-line method offers the option of using all diffraction peaks to calculate the crystallite size of CeO_2-500 and SnO_2-450. Eq.(18SI) can be re-formulated in novel expression as follows Eq.(22SI) [84]. The plot of ($\cos\theta_{hkl}$) as the y-axis versus ($1/\beta_{hkl}$) as the x-axis for corresponding to each diffraction peak of CeO_2-500 and SnO_2-450 are presented in Figs. 3a and 3b, respectively. These are graphs of straight lines with a slope of $k\lambda/D$. The estimated crys-

Table 3. Crystallographicv parameters of the CeO_2-500 NPs obtained by SM and SEAM crystalline size methods.

θ_{hkl} (deg)	β_{hkl} (deg)	θ_{hkl} (ad)	β_{hkl} (rad)	D_{XRD} (nm)	Average D_{XRD} (nm)	δ (nm^{-1})	Average δ (nm^{-1})	ε	Average ε	d-spacing (Å)	*hkl*
28.58	0.7654	0.2433	0.0133	10.06		0.0098		0.0032		3.12	111
33.11	0.751	0.2888	0.0131	10.14		0.0097		0.0031		2.70	002
47.51	0.8697	0.4144	0.0151	8.36	8.71	0.0142	0.0139	0.0034	0.0033	1.91	022
56.37	0.9029	0.4916	0.0157	7.75		0.0166		0.0034		1.63	113
59.13	0.953	0.5158	0.0166	7.25		0.0190		0.0036		1.56	222

Table 4. Crystallographicv parameters of the SnO_2-450 NPs obtained by SM and SEAM crystalline size methods.

$2\theta_{hkl}$ (deg)	β_{hkl} (deg)	θ_{hkl} (rad)	β_{hkl} (rad)	D_{XRD} (nm)	Average D_{XRD} (nm)	$\delta * 10^{-5}$ (nm^{-2})	Average $\delta * 10^{-5}$ (nm^{-2})	$\varepsilon * 10^{-4}$	Average $\varepsilon * 10^{-4}$	d-spacing (Å)	*hkl*
26.6041	0.3555	0.2320	0.0062	22.97		189.5888		2.1526		3.3493	110
33.8862	0.4298	0.2955	0.0074	19.33		267.7686		2.1018		2.6443	101
37.9643	0.391	0.3311	0,0068	21.49		216.5550		2.0711		2.3691	200
38.981	0.433	0.3400	0.0075	19.46		263.9394		2.0635		2.3096	111
51.7772	0.4357	0.4516	0.0076	20.27		243.4137		1.9654		1.7649	211
54.7714	0.4336	0.4777	0.0075	20.64	18.46	234.8424	318.2376	1.9348	1.9356	1.6753	220
57.841	0.645	0.50450	0.0112	14.07		504.9857		1.9073		1.5935	200
61.9095	0.4987	0.5399	0.0086	18.58		289.7982		1.8695		1.4981	310
64.7198	0.721	0.5645	0.0125	13.04		587.7156		1.8444		1.4397	112
65.9565	0.532	0.5752	0.0092	17.80		315.5846		1.8350		1.4157	301
71.271	0.614	0.6216	0.0107	15.92		394.6095		1.7797		1.3226	202
78.7036	0.572	0.6864	0.0099	17.6		310.0492		1.7024		1.2152	321

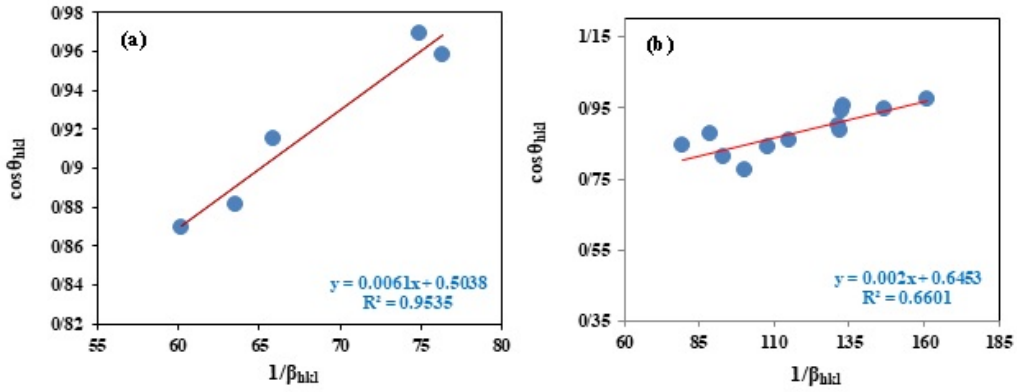

Figure 3. ($\cos\theta_{hkl}$) versus ($1/\beta_{hkl}$) plots of CeO_2-500 (a) and SnO_2-450 (b).

tallite size D_{XRD} was 22.72 and 69.30 nm for CeO_2-500 and SnO_2-450 , respectively. This model is inaccurate since the obtained values of D_{XRD} are higher than those of SM and SEAM (see Tables 3 and 4) [85].

3.6 Sahadat-Scherrer Model (SSM)

The above-listed models face numerous drawbacks in terms of crystallite growth since they yield immense crystallite sizes. So, this model introduces an exact estimation of the crystallite size through forcing the straight line plot to go across the origin [86]. Eq.(23SI) expresses this SSM model. From Figs. 3a and 3b, (x, y) points were obtained and are presented in Table 5. The linear plots have a slope value of $k\lambda/D$ and a negative value of R^2 of -0.438 for for CeO_2-500 (Fig. 4a). and -3.972 for SnO_2-450 (Fig. 4b), which shows the high-scattered data; thus, CeO_2-500 and SnO_2-450 were not scattered perfectly [87]. Crystallite sizes D_{XRD} of 10.344 and 19.25 nm were obtained from slopes for CeO_2-500 and SnO_2-450, respectively. Even though this model yielded a more reasonable value of crystallite sizes, the SSM method is not accurate due to the negative value of the actual R^2. Therefore, the obtained value of R^2 and highlights that CeO_2 NPs were not dispersed perfectly.

3.7 Monshi scherrer method (MSM)

Monshi-Scherrer method provides a more accurate essessment of the crystallite size from all or some exceptional XRD peaks. The mathematical equation can be given as follows: Eq.(24SI) [88]. By reorganizing Eq.(24SI) and setting logarithm on its both sides, yielding to Eq.(25SI). By plotting ($\ln\beta_{hkl}$) versus $\ln(1/\cos\theta_{hkl})$, the typical MSM plots for CeO_2-500 and SnO_2-450 are obtained , as illustrated in Figs. 5a and 5b, respectively. The linear fitting lines determined from Eq.(25SI) were achieved which has the intercept of $\ln(k\lambda/D_{XRD})$ Eq.(26SI). This equation Eq.(26SI) is converted into exponential form, then we get Eq.(27SI). Using Eq.(27SI), the crystallite size D_{XRD} of CeO_2-500 and SnO_2-450 can be estimated as 11.26 and

Table 5. (x,y) points obtained from Figs. 3a and 3b.

CeO_2-500	Values of x	0.869	0.881	0.915	0.958	0.969							
	Values of y	0.0116	0.0118	0.0122	0.01287	0.0129							
SnO_2-450	Values of x	161.25	133.38	146.61	132.39	131.57	132.21	88.88	114.95	79.51	107.75	93.36	100.22
	Values of y	1.16	0.96	1.06	0.95	0.95	0.95	0.64	0.83	0.57	0.78	0.67	0.72

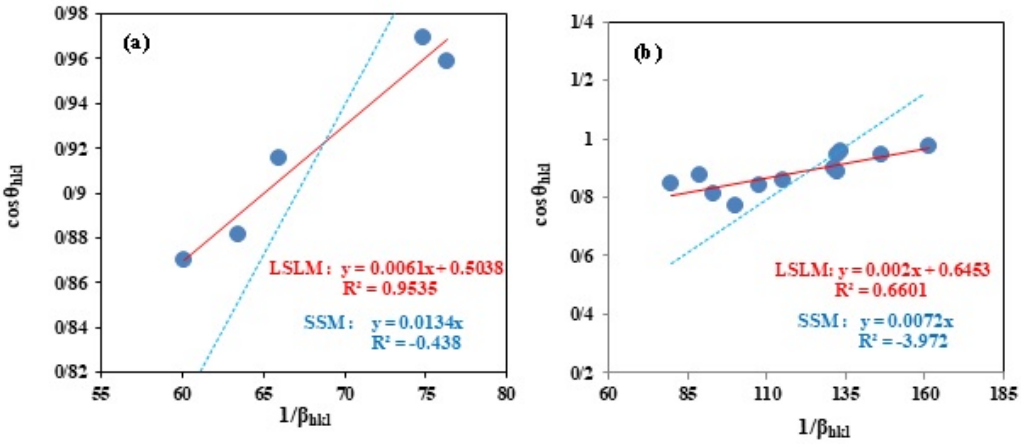

Figure 4. ($\cos\theta_{hkl}$) versus $1/\beta_{hkl}$ plots of CeO_2-500 (a) and SnO_2-450 (b).

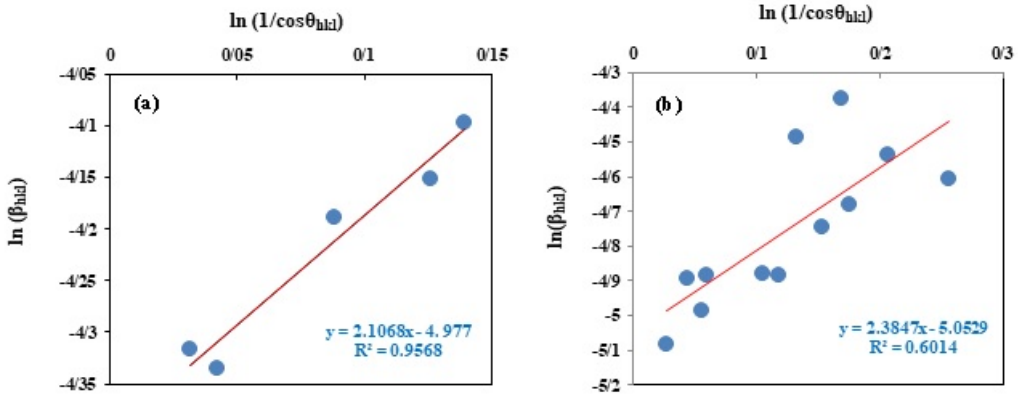

Figure 5. ($\ln \beta_{hk}$) versus ln ($1/\cos \theta_{hkl}$) plots of CeO_2-500 (a) and SnO_2-450 (b).

21.68 nm, respectively, which are almost close to the values obtained through the SM and SEAM methods.

3.8 Williamson-Hall method (WHM)

One of the methods considering the impact of the lattice strain on the broadening of the XRD peaks is the Williamson–Hall method (WHM). This model excluded the $1/\cos\theta$ dependency by introducing the variation with $\tan\theta$ in strain considerations [89]. The imperfections and/or distortions in the crystals are the driving force of strains. So, the total broadening (β_{hkl}) due to size (β_{size}) and strain (β_{strain}) in a particular peak having the Miller indices h, k, and l can be written as Eq.(28SI).

3.8.1 Uniform deformation model (UDM)

The expression of the β_{strain} is described as Eq.(29SI) [90], and that of the β_{size} is given by Eq.(30SI). Thus, β_{hkl} is given by the following relation Eq.(31SI). Both sides of Eq.(31SI) are multiplied by the same term ($\cos\theta_{hkl}$), and knowing that $\sin\theta_{hkl} = \tan\theta_{hkl} \times \cos\theta_{hkl}$, the resulting formula could be obtained Eq.(32SI). The standard equation for a straight line Eq.(33SI) is compared with the extrapolated linear portion of the previous equation Eq.(32SI).

By drawing ($\beta_{hkl}.\cos\theta_{hkl}$) versus ($4\sin\theta_{hkl}$), linear equations ($y = 0.00106x + 0.0111$ and R^2 of 0.8588) and ($y = 0.0016x + 0.0048$ and R^2 of 0.3451) were achieved for CeO_2-500 (Fig. 6a) and SnO_2-450 (Fig. 6b), respectively. The crystallite size D_{XRD} values were determined from intercepts ($K\lambda/D_{XRD}$) of approximately as 12.48 nm [91] for CeO_2-500 and 28.67 nm [92] for SnO_2-450 Meanwhile, the intrinsic strains were calculated from slopes (ε) of the linearly fitted data, as 1.16×10^{-3} [93] and 1.6×10^{-3} for CeO_2-500 and SnO_2-450, correspondingly. The predicted results are tabulated in Tables 7 and 8. The positive slope values represented the tensile strain in the nanocrystals. By taking into account the fit (R^2), it could be highlighted that data points slightly deviated from the plotted straight line for CeO_2-500, while the divergence between experimental and predicted data was more sensitive in the case of SnO_2-450, signaling a high-dispersed data which could be explained by substantial dislocations and stacking faults effects.

3.8.2 Uniform stress deformation model (USDM)

This adjusted model is pertinent to describe the homogeneity and anisotropic nature of lattice stress investigation in all crystallographic orientations, according to the generalized Hooke's law [94]. Generally, for small deformations, the stress (σ) and strain (ε) of the crystal are proportional to each other, and this is known as Hooke's Law Eq.(34SI). Thus, using Eq.(34SI), the adjusted WHM for USDM can be written as Eq.(35SI) [95]. Young's modulus Y_{hkl} for CeO_2-500 with cubic structural material is related to their three elastic compliance constants (S11, S12, and S44) [96] and Miller indexes of the crystallographic plane (h,k, and l) as Eq.(36SI). Compliance is the inverse of stiffness. Thus, the compliances of a cubic crystal can be calculated from the

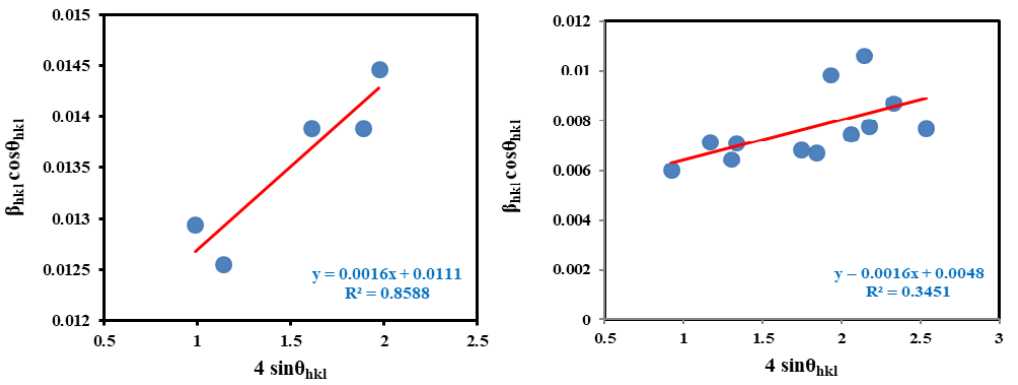

Figure 6. ($\beta_{hkl}.\cos\theta_{hkl}$) versus ($4\sin\theta_{hkl}$) plots of CeO_2-500 (a) and SnO_2-450 (b).

Table 6. Elastic compliances and stiffness constants of CeO2-500 and SnO2-450.

	Stiffness constants (GPa)						Elastic compliances $(GPa^{-1})*10^{-3}$					
CeO_2-500	C_{11}	C_{12}	-	-	C_{44}	-	S_{11}	S_{12}	-	-	S_{44}	-
	455	190	-	-	81.5	-	2.90	-0.851	-	-	12.3	-
SnO_2-450	C_{11}	C_{12}	C_{13}	C_{33}	C_{44}	C_{66}	S_{11}	S_{12}	S_{13}	S_{33}	S_{44}	S_{66}
	261.70	177.20	155.5	449.6	103.7	207.4	7.4260	-4.4080	-1.0438	2.9460	9.7000	4.8216

Table 7. Geometric parameters (D_{XRD}, δ, ε, σ, U, SAA, n, and R^2) for CeO_2-500 using various methods.

SI. N°.	Methods	Abbr.	D_{XRD} (nm)	δ (nm^{-2})	$\varepsilon \times 10^{-4}$	$\sigma \times 10^{7}$ (Pa)	$U \times 10^{3}$ (kJ/m^3)	SAA (m^2/g)	n	R^2
1	Scherrer method	SM	10.06	0.01	32	-	-	82.58	3366.232	-
2	Scherrer equation average method	SEAM	8.75	0.014	33	-	-	95.32	2188.467	-
3	Linear straight-line method	LSLM	22.72	0.0019	-	-	-	36.56	38789.688	0.9535
5	Monshi scherrer method	MSM	11.26	0.0078	-	-	-	73.75	4724.940	0.9605
4	Sahadat-Scherrer model	SSM	10.34	0.0093				80.31	3659.244	-0.438
6	Williamson-Hall plot method	UMD	12.48	0.0064	16	-	-	66.53	6437.791	0.8588
		USDM	12.48	0.0041	-	10.00	-	66.53	6437.791	0.8588
		UDEDM	11.00	0.0045	2.25	1.93	2.17	75.52	4401.434	0.9325
7	Size-strain plot method	SSPM	11.36	0.0077	1090	-	-	73.12	4848.711	0.9975
8	Halder-Wagner method	HWM	11.36	0.0077	25	-		73.12	4848.711	0.9975

S.I.: Sample identification; Abbr.: Abreviation

Table 8. Geometric parameters (D_{XRD}, δ, ε, σ, U, SAA, n, and R^2) for SnO_2-450 using various methods.

SI. N°.	Methods	Abbr.	D_{XRD} (nm)	$\delta \times 10^{-3}$ (nm^{-2})	$\varepsilon \times 10^{-4}$	$\sigma \times 10^{-4}$ (TPa)	$U \times 10^{3}$ (kJ/m^3)	SAA (m^2/g)	$n \times 10^{3}$	R^2
1	Scherrer method	SM	22.97	1.9	2.1	-	-	37.42	88.3968	-
2	Scherrer equation average method	SEAM	18.46	3.2	1.9	-	-	46.57	45.8826	-
3	Linear straight-line method	LSLM	69.30	0.21	-	-	-	12.40	2427.4677	0.6601
5	Monshi scherrer method	MSM	21.69	2.1	-	-	-	39.63	74.4273	0.6014
4	Sahadat-Scherrer model	SSM	19.25	2.7				44.65	52.0290	-3.972
6	Williamson-Hall plot method	UMD	28.88	1.2	16	-	-	29,76	175.6893	0.3451
		USDM	28.88	1.2	15	3.00	0.226	29.76	175.6893	0.3451
		UDEDM	28.29	1.25	58	11.6	0.250	30.39	165.1401	0.4535
7	Size-strain plot method	SSPM	23.89	1.8	918	-	-	35.98	99.4494	0.9031
8	Halder-Wagner method	HWM	23.89	1.8	22	-		35.98	99.4494	0.9031

S.I.: Sample identification; Abbr.: Abreviation

elastic stiffness constant C_{11}, C_{12}, and C_{44} using the following relationships: Eq.(37SI), Eq.(38SI), and Eq.(39SI).The elasticity stiffness C_{11}, C_{12}, C_{44} [97] for Cubic CeO_2-500 are displayed in Table 6. Hence, the elastic compliance values have been determined as S_{11}=2.904×10^{-3}, S_{12} =-0.8513×10^{-3}, and S_{44}=12.27×10^{-3} GPa and then the Young's modulus Y_{hkl} for different orientations. Seeing that ceria nanocrystals are elastically anisotropic, the average value of the predicted Young's modulus for CeO_2-500 has as ∼ 860 GPa. The elasticity stiffness and the elastic compliance values of cubic CeO_2-500 are presented in Table 6. Considering a tetragonal structural material, Young's modulus Y_{hkl} for SnO_2-450 is associated with their five elastic compliance constants (S_{11}, S_{12}, S_{13}, S_{33}, S_{44}, and S_{66}) [98] which is expressed as follows Eq.(40SI). Elastic compliances of the SnO_2-450 can be computed from the elastic stiffness constants (C_{11}, C_{12}, C_{13}, C_{33}, C_{44}, and C_{66}), as tabulated in Table 6, and by using the following equations Eqs.(41SI-47SI). Therefore, the elastic compliances values have been calculated as S_{11} = 7.426, S_{12} = -4.408, S_{13} = -1.0438, S_{33} = 2.946, S_{44} = 9.7 and S_{66} = 4.8216. Using these compliances values, the Young's modulus value have been calculated for different (h k l) planes and the average value of the predicted Young's modulus for SnO_2-450 has as ∼ 200 GPa since the tin oxide nanocrystals are elastically anisotropic, as presented in Table 6.

By tracing plots ($\beta_{hkl}.\cos\theta_{hkl}$) against ($4\sin\theta_{hkl}/Y_{hkl}$) corresponding to the XRD patterns for CeO_2-500 (Fig. 7a) and SnO_2-450 (Fig. 7b), straight-line equations (y =$10^{-8}x$ +0.0111 and R^2 of 0.8588) for CeO_2-500 and (y =00003x +0.0048) and R^2 of 0.3451) for SnO_2-450 are observed on these plots. The slope of these provides the values of stress,

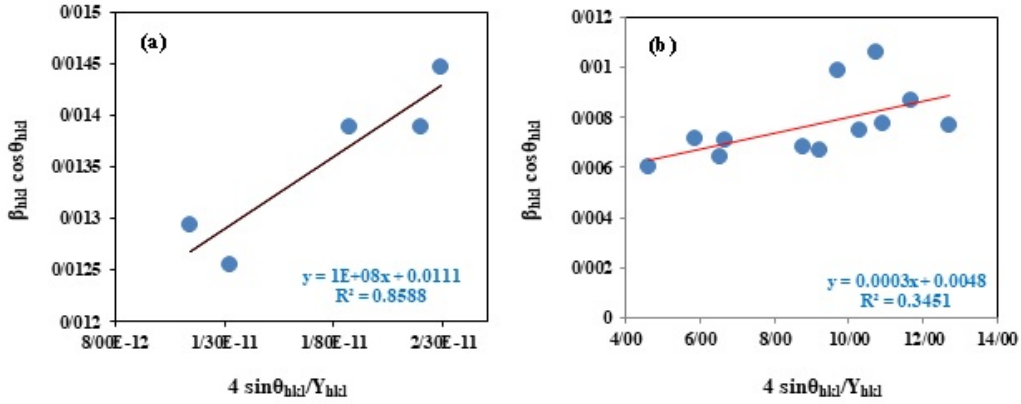

Figure 7. (β_{hkl}.cos θ_{hkl}) versus (4sin θ_{hkl}/Y$_{hkl}$) plots of of CeO_2-500 (a) and SnO_2-450 (b).

whereas they give the average particle size of the CeO_2-500 and SnO_2-450. The crystallite size D_{XRD} was calculated from the intercepts of the straight lines as 12.4873 nm [99] and 28.88 nm [100], respectively. Meanwhile, the premeditated uniform deformation stress from the slopes are approximately 108 Pa and 3×10^{-4} TPa, by taking into account Y_{hkl} value (E_{hkl} ~ average Young's modulus as ~ 86 GPa for CeO_2-500 and 200 GPa for SnO_2-450). Here also we could highlight the availability of dislocations and stacking faults effects in the both catalysts as it was evidenced in the high- scattered experiment and low value of R^2. Thus, the USDM model is not accurate, especially for SnO_2-450.

3.8.3 Uniform deformation energy density model (UDEDM)

This model is a theoretical prototype for estimating a crystal's energy density through considering uniform anisotropic lattice strain in all crystallographic orientations [101]. The relationship between energy density (u) and strain (ε) is presented as Eq.(48SI). The energy density (u) and stress (σ) are connected by the following equation Eq.(49SI). Therefore, Hooke's law could be concluded from the association of Eq.(48SI) and Eq.(49SI), Eq.(50SI). By using Hooke's law Eq.(50SI), the modified WHM for the UDEDM model can be transcribed as Eq.(51SI). Graphs of (β_{hkl}.cos θ_{hkl}) versus (4sin θ_{hkl} $(2/Y_{hkl})^{1/2}$) were plotted for CeO_2-500 and SnO_2-450, as shown in Figs. 8a and 8b, respectively. Straight-line equations (y= 46.607x+0.0126 and R^2=0.9325 for CeO_2-500) and (y= 0.00and 05x+0.0049 and R^2 =0.4535 for SnO_2-450) are observed on these plots. The corresponding crystallite sizes D_{XRD} was determined from intercepts ($k\lambda/D_{XRD}$), whereas the energy density (u) from slopes ($u^{1/2}$) of the plotted graphs as 11.00 nm [102] and 2.17×10^3 kJ/m^3 for CeO_2-500 and 28.28 nm [103] and 250 kJ/m^3 for SnO_2-450, as displayed in Table 6. The strain could be determined by knowing the E_{hkl} value (E_{hkl} ~ average Young's modulus) of the CeO_2-500 and SnO_2-450 NPs by the Eq.(48SI). Results showed that the strain values (ε) were 2.25×10^{-4} for CeO_2 and 1.58×10^{-3} for SnO_2-450 NPs, suggesting that the strains obtained were tensile, as the values were positive. Further, the stress could be estimated from Eq.(49SI), i.e.1.93×10^7 kJ/m^3 for CeO_2-500, and from Eq.(42SI), i.e., 3.16×10^{-4} TPa for SnO_2-450. Besides, the UDEDM model exhibited the smallest values of crystallite size intrinsic strain for CeO_2-500, implying that lattice strain was anisotropic in nature. It is obvious that for both materials, Williamson-Hall models result in almost the same microstructure parameters (D_{XRD}, δ, ε, and u). Besides, the values of R^2 were highest for CeO_2-500 but smallest for SnO_2-450, an indication of the low scattered data in the former and high dispersed experiment points in the latter. Thus, Williamson-Hall models of are not realistic for SnO_2-450. Based on the closed crystallite sizes obtained by the Scherrer methods (SM, SEAM,

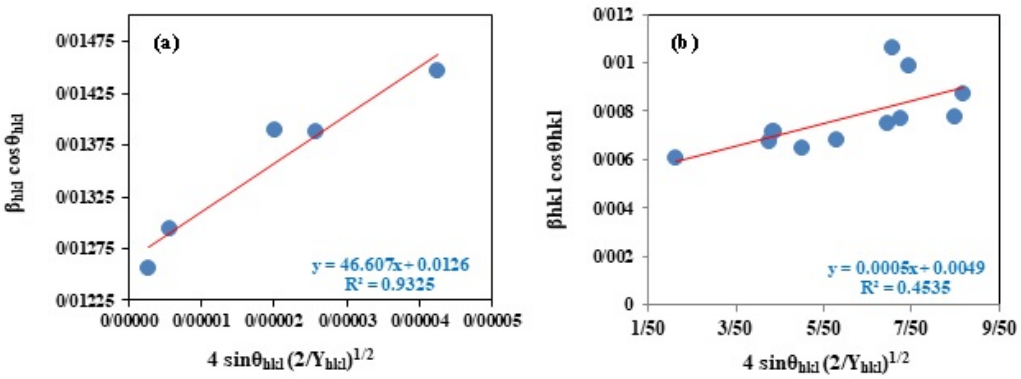

Figure 8. (β_{hkl}.cos θ_{hkl}) versus (4sin θ_{hkl} $(2/Y_{hkl})^{1/2}$) plots of CeO_2-500 (a) and SnO_2-450 (b).

MSM), various W–H models, SSPM, and HWM methods, we concluded that there is no significant strain in the lattice of the as-synthesized CeO_2-500 NPs sample [104].

3.9 Size-strain plot method (SSPM)

In the SSPM approach, the size profile is defined by the Lorenztian function (β_L) whereas strain broadening is described by the Gaussian function (β_G) [105]. So, the total widening (β_{hkl}) is the combination of broadening based on Lorentzian (β_L) and Gaussian (β_G) functions, as follow Eq.(52SI). So, the SSPM plot is represented by the following equation: Eq.(53SI) [106]. To follow the dimensional consistency rule, we multiply the term ($\varepsilon/2$) in the second side of Eq.(53SI) by λ , and we get the respective equation Eq.(54SI). Now, using Eq.(54SI), plots can be drawn $(d_{hkl}.\beta_{hkl}.\cos\theta_{hkl})^2$ versus $(d_{hkl}^2.\beta_{hkl}.\cos\theta_{hkl})$ respective to each diffraction peak of CeO_2-500 and SnO_2-450, which are shown in Fig. 9a and Fig. 9b, respectively. Their straight-line equations (y= 0.0122x+7×10^{-5} and R^2 = 0.9975) and (y= 0.0058x+5×10^{-5} and R^2 of 0.9031), respectively. The crystallite sizes of both catalysts were premeditated from slopes ($K\lambda/D_{XRD}$) as 11.36 nm [107] and 23.89 nm [108] for CeO_2-500 and SnO_2-450, respectively, while the intrinsic strain was computed from intercepts $(\varepsilon\lambda/2)^2$ expressing the values of 0.109 for CeO_2-500 and 0.092 for SnO_2-450. These lattice strains with positive values mean that the crystals have a tensile strain. Additionally, SSPM presented the highest values of R^2 and significant strains, which would suggest the narrower size distribution and maybe the presence of defects and size-shape anisotropy in the CeO_2-500 and SnO_2-450 materials. Thus, we suggest that the SSPM method is more accurate for both materials.

3.10 Halder-Wagner method (HWM)

Halder-Wagner Method is devots to describe β_{hkl} of the physical profile in consistency with the Voigt function [109] as follows Eq. (55SI). Besides, Halder-Wagner model is stated as Eqs.(56-68SI). Amalgamation and rearrangement of Eqs.(56-58SI) yield Eq.(59SI).
The plots of $(\beta_{hkl}/\tan\theta_{hkl})^2$ versus $(\beta_{hkl}\cos\theta_{hkl}/\sin 2\theta_{hkl})$ for each peak of the XRD patterns of CeO_2-500 (Fig. 10a) and SnO_2-450 (Fig. 10b) were performed. The linear fitting of the plots results in slope ($K\lambda/D_{XRD}$) values of 0.0122 for CeO_2-500 and 0.0058 for SnO_2-450. Thus, the calculated crystallite sizes are 11.36 nm [110] and 23.89 nm [111] for CeO_2-500 and SnO_2-450, correspondingly. In addition, the premeditated values of intrinsic strain from the intercepts of the plots ($16\varepsilon^2$) is found out to be 2.5×10^{-3} (CeO_2-500) and 2.2×10^{-3} (SnO_2-450, emphasizing that the strains obtained were tensiles, since the values were positives. In comparison with the SSPM model, the HWM model gave the highest R^2 and exhibited a decrease in the intrinsic strain , which indicates the narrower size distribution, trivial strains, and the presence of defects and size-shape isotropy in the CeO_2-500 and SnO_2-450 environment. These findings highlight that the HWM model is the most accurate for

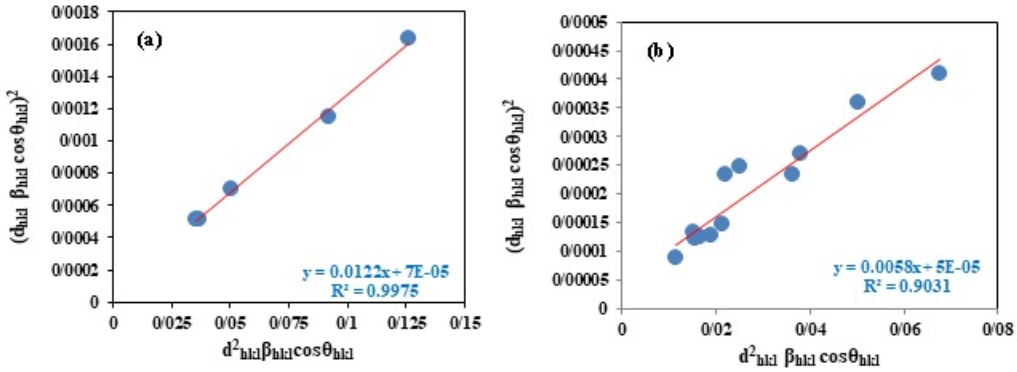

Figure 9. $(d_{hkl}.\beta_{hkl}.\cos\theta_{hkl})^2$ versus $(d_{hkl}^2.\beta_{hkl}.\cos\theta_{hkl})$ plots of CeO_2-500 (a) and SnO_2-450 (b).

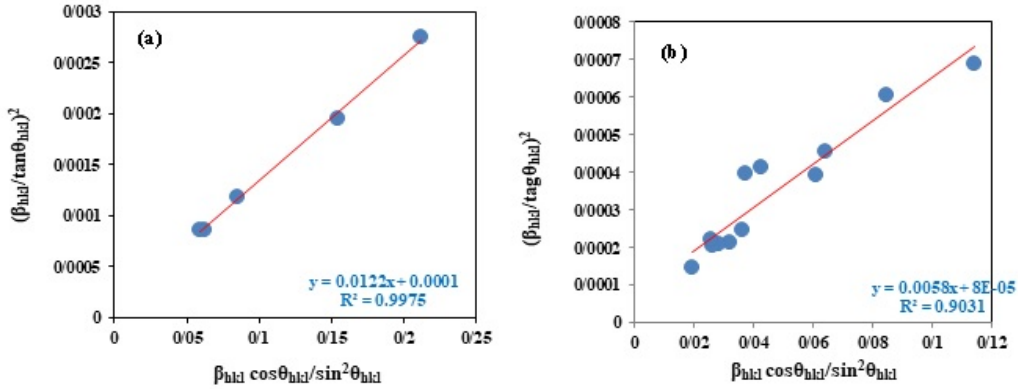

Figure 10. $(\beta_{hkl}/\tan\theta_{hkl})^2$ versus $(\beta_{hkl}\cos\theta_{hkl}/\sin^2\theta_{hkl})$ plots of CeO_2-500 (a) and SnO_2-450 (b).

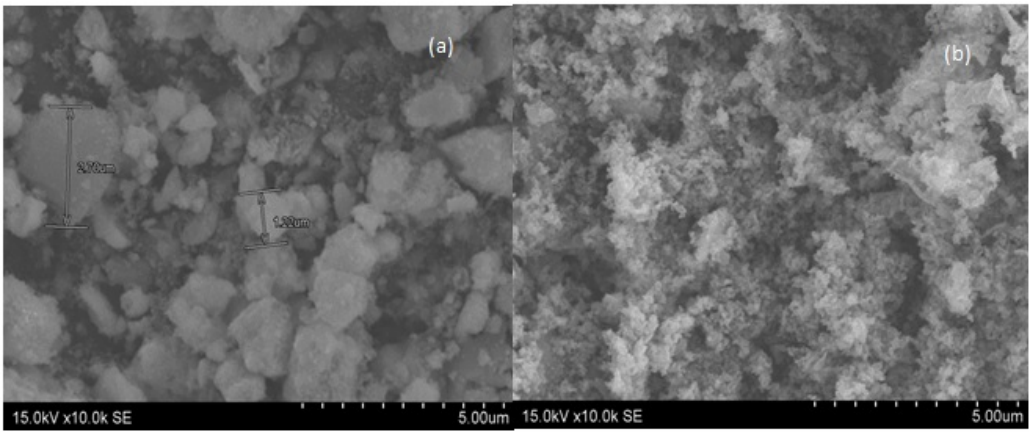

Figure 11. SEM images of CeO_2-500 (a) and SnO_2-450 (b).

CeO_2-500 as well as SnO_2-450 materials. Tables 7 and 8 displayed the geometric parameters (D_{XRD}, δ, ε, σ, U, SAA, n, and R^2) for the examined CeO_2-500 SnO_2-450 catalysts using various available methods.

3.11 Morphological analysis

Fig. 11a illustrates a typical SEM image of CeO_2-500. It shows the occurrence of arbitrarily distributed aggregates of CeO_2-500 NPs with dimensions of about 100 and 300 nm along with ultrafine NPs with sizes up to 300 nm, which favor spherical particles [112] to further reduce the surface energy [113]. SEM micrograph of SnO_2-450 is depicted in Fig. 11b revealing the presence of foamely NPs structures which caused by the gas release upon decomposition [114].

3.12 UV-Vis DRS analysis

The absorption spectra and estimation of bandgap energy for CeO_2-500 (Figs. 12a and 12b) and for SnO_2-450 (Figs. 13a and 13b) were presented. As shown in (Fig. 12a), CeO_2-500 illustrates two absorption bands in the ultraviolet domain, positioned at ≈255 nm (4.86 eV) and ≈ 355 nm (3.49 eV), which may be attributed to the transitions from the O 2p

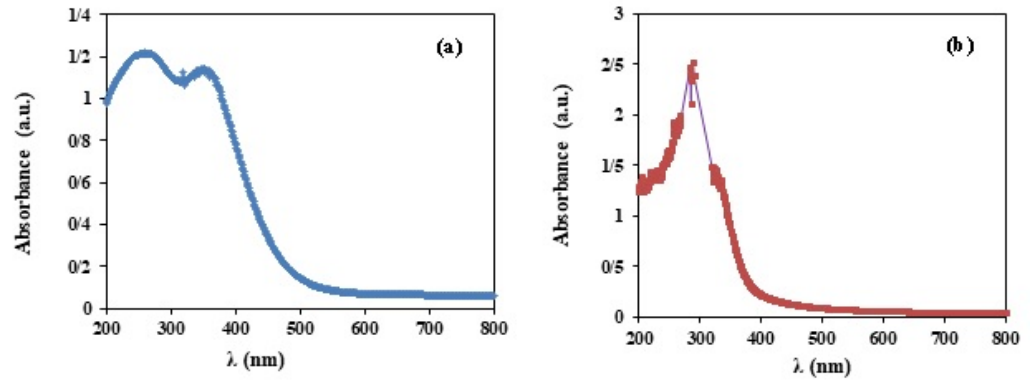

Figure 12. Optical spectra of CeO_2-500 (a) and SnO_2-450 (b).

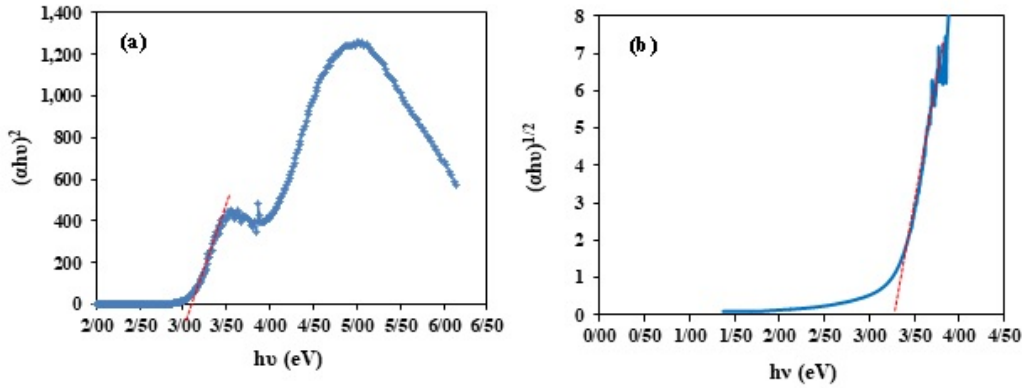

Figure 13. $(\alpha h\nu)^2$ versus $(h\nu)$ plots of CeO_2-500 (a) and SnO_2-450 (b).

state (VB) to Ce 5d state (CB) and from the O 2p state (VB) to the localized Ce 4f state, respectively. On the other hand, SnO_2-450 (Fig. 12b), also displayed two different absorption bands are placed approximatively in the 210 – 245 nm scale, originating from the charge-transfer transition between the O 2p and Sn 4d states in O^{2-} and Sn^{4+}, and 270 – 285 nm range, attributing, either to the inter-valence transition of Sn^{4+}/Sn^{2+} or to the charge-transfer transition of Sn^{2+} ions [115]. The modified Schuster-Kubelka-Munk-M function Eq. 1 was used to assess the energy band gap (E_g) for each catalyst [116].

$$(\alpha h\nu)^{1/n} = A(h\nu - E_g) \tag{1}$$

where α, $h\nu$, E_g, A, and n are the absorption coefficient, the photon energy, the band gap energy of the material, a constant, and the nature of semiconducting material depending upon the transition mode (for direct allowed transition n=0.5 and for indirect allowed transition n=2).

By tracing $(\alpha h\nu)^{1/n}$ versus $(h\nu)$ as per Eq. 1 and assuming that both materials behave as a direct allowed transition (n=0.5) semiconductors, the E_g of the CeO_2-500 and SnO_2-450 were computed from the straight lines x-intercept of the graphs plotted for CeO_2-500 (Fig. 13a) and SnO_2-450 (Fig. 13b) approximatively as 3.10 eV [117] and 3.35 eV [118], respectively. The obtained E_g , as listed in Table 9, exhibited a blue shift compared to these reported for the bulk CeO_2 (3.15 eV) and SnO_2 (3.6 eV) due to the quantum confinement effect [119].

The VB edge energy (E_{VB}) of both CeO_2-500 and SnO_2-450 can be computed from the following mathematical expression Eq. 2 [120],

$$E_{VB} = \chi - E^C + 0.5E_g \tag{2}$$

The CB edge energy (E_{CB}) of the semiconductor materials can be estimated as follows: Eq. 3.

$$E_{CB} = E_{VB} - E_g \tag{3}$$

where χ is the absolute electronegativity of the semiconductor (eV), E_g is the band gap energy of the semiconductors (for CeO_2-500 E_g=3.10 eV and for SnO_2-450 E_g=3.35 eV), and E^C is the energy of free electrons in hydrogen scale (4.5 eV).

According to Mullikan electronegativity concept, the molecular electronegativity of semiconductors (χ), which is roughly the geometric mean of the electronegativities of the isolated atoms, can be determined using the following equation Eq. 4 [121].

$$a\chi = \prod_{i=1}^{n} (\chi_i^{a_i})^{1/a_i} \tag{4}$$

where χ_i is the absolute electronegativity of each constituent atom i, which is defined as the average arithmetic mean of the atomic electron affinity (E_a) and the first ionization energy (E_i) for constituent atom i and ai is the number of atoms in the compound i.

The concept of electronegativity is explored for AB_2-type oxide semiconductor, forming a chemical bond between two different atoms (A-B). Thus, Eq. 4 can be re-written in novel expression as follow Eq. 5.

$$\chi = [(\chi_A)^a(\chi_B)^b]^{1/a+b} \tag{5}$$

(χ_A) and (χ_B) are the electronegativities of isolated atoms A and B, and the exponential a, and b are the semiconductor' number of atoms A and B, respectively. In the case of CeO_2-500 and SnO_2-450, the data used and results obtained are tabulated in Table 10.

3.13 Computational details

Fig. 14 illustrates the geometry optimization of CR molecule using the Gaussian-09 revision -D01-SMP program using DFT at B3LYP/6-31G* level. The estimated theoretical reactivity parameters (E_{HOMO}, E_{LUMO}, E_g, η, μ and ω) of CR are displayed in Tables 10.

3.14 Photocatalytic degradation of CR dye

Five preliminary assays were carried out to optimize the photocatalytic degradation effectiveness of these materials

Table 9. Data used in the computation of VB and CB-potential positions for CeO_2-500 and SnO_2-450 NPs

Mullikan electronegativity of the constituent elements				
Element	E_a (eV)	E_i (eV)	$\frac{1}{2}(E_a+E_i)$ (eV)	
Ce	0.57	5.538	3.054	
Sn	1.112	5.538	4.228	
O	1.461	13.618	7.539	
Band gap energies and potential positions of VB and CB of the used semiconductors CeO_2-500 and SnO_2-450				
S.I.	χ (eV)	E_g (eV)	E_{CB} (eV)	E_{VB} (eV)
$CeO_2$500 NPs	5.56	3.10	-0.49	2.61
$SnO_2$500 NPs	≈6.25	3.35	≈0.08	≈3.43

S.I.: Sample identification

Table 10. Represented E_{HOMO}, E_{LUMO}, E_g, η. μ and ω of CR dye.

Molecule	E_{HOMO} (eV)	E_{LUMO} (eV)	E_g (eV)	η (eV)	μ (eV)	ω (eV)
CR	-4.76	-1.78	2.48	1.24	-3.02	3.67

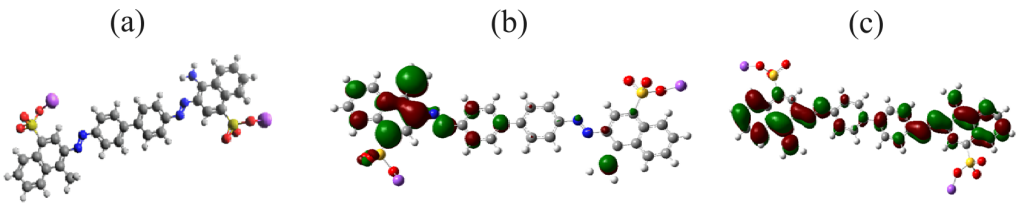

Figure 14. (a) Optimized structure, (b) HOMO and (c) LUMO orbitals for CR dye.

towards CR azodye, including self-photolysis (CR/UVA process), adsorption (CR/ CeO_2-500 and CR/SnO_2-450 systems) and heterogeneous photocatalysis (CR/ CeO_2-500/UVA and CR/ SnO_2-450/UVA processes), as presented in Fig. 15 along with crystallographic, physical, optical, photolysis, adsorption and photocatalytic parameters of CeO_2-500 and SnO_2-450NPs. Consequently, after illumination for 100 min, 76.44% CR for CeO_2-500 NPs and 61.53% CR for SnO_2-450NPs were achieved. Basically, the increased photo-sensibility of these materials was primarily accredited to the mono-dispersed particle size $\approx 10-12$ (CeO_2-500) and $20-30$ nm (SnO_2-450), high crystallinity, less particles agglomeration, great surface-to-volume ratio, appropriate position of energy levels of edges E_{VB} and E_{CB},, strong reversible Ce^{3+}/Ce^{4+} and Sn^{2+}/Sn^{4+} redox, and appropriate light-harvest action ability. Furthermore, the large number of surface Ce^{3+}-O and Sn^{2+}-O defects sites serve as electrons trapping sites which can boost the separation effectiveness of electron-hole pairs and thus ultimately increases the degradation rate. These reactive oxygen species (ROS) species (O_2• -, •OH) and redox systems (Ce^{3+}/Ce^{4+} and Sn^{2+}/Sn^{4+}) along with oxygen vacancies are supposed to be oxidative driving forces of destruction target pollutants [122]. Conversely, negligible degradation of 0.49% CR was obtained under UVA-irradiation only while adsorption efficiency η= 50% and η=65% CR were reached by CeO_2-500 and SnO_2-450 under dark conditions, respectively [123]. Accordingly, CeO_2-500 and SnO_2-450 NPs catalysts demonstrate excellent features, resulting in an efficient photo-induced electron-hole separation as well as boosting the photocatalytic conversion process.

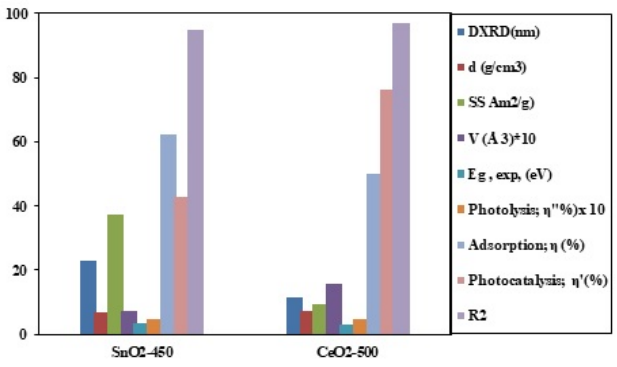

Figure 15. Crystallographic. physic. optic. Photolysis. Adsorption. photocatalytic parameters of CeO_2-500 and SnO_2-450. ([nano-catalyst] =0.5 g/L, [CR]=20 mg/L, pH= 7 (for CeO_2) and 8 (for SnO_2), T=25 °C), λ_{max} = 365 nm, Intensity = 90 J. cm^{-2} and irradiation time = 100 min).

To adequately explain the photo-degradation kinetics of heterogeneous catalytic systems, the Monomolecular Langmuir–Hinshelwood kinetic equation is given by Eq. 6 [124]

$$r = -(\frac{dC}{dt}) = K_{app}C_0 = \frac{K_1K_2C_0}{1+K_2C_0} \tag{6}$$

where r represents the rate of reaction that changes with time (mg/(L.min), K_1 (L/min) is a specific rate constant that changes with photocatalytic activity, K_2 (L/mg) the adsorption equilibrium constant, and C_0 is the initial concentration of the substrate (mg/L) . Inversion of the above rate equation is given by Eq. 7:

$$\frac{1}{K_{app}}(\frac{1}{C_0}) = (\frac{1}{K_1K_2}) + (\frac{1}{K_1})C_0 \tag{7}$$

Thus, a plot $1/K_{app}$ against C_0 should be a straight line with a slope of $1/K_1$ and an intercept of $1/(K_1K_2)$. Such analysis allows one to quantify the photocatalytic activity of the catalyst through the specific rate constant K_1 (with larger K_1 values corresponding to higher photocatalytic activity) and adsorption equilibrium constant K_2 (K_2 expresses the equilibrium constant for fast adsorption-desorption processes between the surface of catalyst and substrates). The integrated form of the above Eq. 7 yields to the following Eq. 8.

$$t = (\frac{1}{K_1K_2})ln\frac{C_0}{C} + \frac{1}{K_2}(C_0 - C) \tag{8}$$

where t is the time (min) required for C_0 to decrease to C. Since the dye concentration is very low, the second term of Eq. 8 becomes small when compared with the first one, and under these conditions, the above equation reduces to Eq. 9.

$$\ln\frac{C_0}{C} = K_1K_2t = K_{app}t \tag{9}$$

where $K_{app} = K_1K_2$ is the apparent pseudo-first-order rate constant (min^{-1}), C and C_0 are the dye concentration before and after irradiation (mg/L) , respectively. The plot of ln C_0/C against t should give straight lines, whose slope is equal to K_{app}.

The kinetic results of the photodegradation of CR by CeO_2-500 and SnO_2-450 were interpreted by plotting ($\ln C/C_0$) versus (t) (graphs of plots not shown). As listed in Table 11, the photodecomposition kinetics were reasonably correlated to the pseudo-first-order model with the high R^2 (0.95 – 0.97)

Table 11. Crystallographic and photocatalytic data (D_{XRD}, d, SSA, V, $E_{g.exp}$, η, η', η'' K_{app} and R^2) of CeO_2-500 and SnO_2-450.

Crystallographic parameters of catalyst*		
	CeO_2	SnO_2
D_{XRD}(nm)	11.36	23.89
d (g.cm^{-3})	7.2103	6.98
SSA(m^2.g^{-1})	93.12	37.42
V ($Å^3$)	158.29	71.75
$E_{g.exp}$, (eV)	31	3.35
Photocatalytic data and kinetic parameters ([nano-catalyst] =0.5 g/L, [CR]=20 mg/L, pH= 7 (for CeO_2) and 8 (for SnO_2), T =25°C), λ_{max} = 365 nm, Intensity = 90 J. cm^{-2} and irradiation time = 100 min).		
Photolysis; η''(%)x10^{-1}	4.5	4.9
Adsorption; η (%)	50	42.94
Photocatalysis; η' (%)	76.44	62.45
K_{app} (min^{-1})x10^{-2}	1	2
R^2 (%)	97	95

* : Crystallographic parameters from Halder-Wagner method ; η (%): Adsorption efficiency ; η' (%): Photocatalytic efficiency; η'' (%): Photolysis efficiency; k_{app}: Apparent pseudo-first order rate constant; R^2; Regression coefficient

3.15 Possible reaction mechanism

On the base of the feature and investigational results discussed previously, we succinctly explain the suggested photocatalysis mechanisms by CeO_2-500 (Fig. 16a) and SnO_2-450 (Fig. 16b) under UVA-light irradiation.The energy of the light excitation (λ_{UVA}=365∓10 nm→E_{UVA}=3.40∓0.1 eV) is sufficient to directly excite the CeO_2-500 (E_g=3.1 eV→ λ_{edge}=400 nm) and SnO_2-450 (E_g=3.35 eV → λ_{edge} =370 nm) as per to the predicted band edge positions of explored materials (Table 9). When the UVA falls on the CeO_2-500 and SnO_2-450 catalysts, electrons (e-) in their VBs transfer to CBs with synchronized production of a similar amount of holes (h^+) (Eq. 10) and Eq. 18, respectively. In the case of CeO_2-500 (Fig. 16a), a part of the photoinduced electrons on CeO_2-500 surface reduced Ce^{4+} to Ce^{3+} Eq. 11. The reduced Ce^{3+} react with O_2 to yield $•O_2^-$ Eq. 12. Meanwhile, stimulated electrons in CB reduce the dissolved O_2 to O_2^- Eq. 13, then to HO_2• Eq. 14 and after that to HO• Eq. 15, because the CB edge potential of CeO_2 (-0.49 eV) is much lower than that of O_2/O_2^- (-0.28 eV). Meanwhile, the VB edge energy of CeO_2 is +2.61 eV, more negative compared to that of H_2O/•OH (+2.8 eV) but much higher than that of OH^-/•OH (+1.99 eV), implying that the excited holes (h^+) in VB of CeO_2-500 cannot competent to react with H_2O to produce •OH radicals. However, they are can easily oxidize HO^- to •OH radicals (Eq. 16. Hence, ROS (•OH and O_2^-) undergo a reaction with CR azodye molecules to form intermediate products and finally mineralize to H_2O and CO_2 (Eq. 17):

$$CeO_2 + h\nu_{(\text{UVA-light})} \rightarrow CeO_2\{e^-_{(CB)} + h^+_{(VB)}\} \quad (10)$$

$$Ce^{4+} + e^-_{(CB)} \rightarrow Ce^{3+} \quad (11)$$

$$Ce^{3+} + O_2 \rightarrow O_2^{\bullet-} + Ce^{4+} \quad (12)$$

$$O_2 + e^-_{(CB)} \rightarrow O_2^{\bullet-} \quad (13)$$

$$O_2^{\bullet-} + H^+ \rightarrow HO_2^{\bullet} \quad (14)$$

$$O_2^{\bullet-} + 4H^+ \rightarrow 2^{\bullet}OH \quad (15)$$

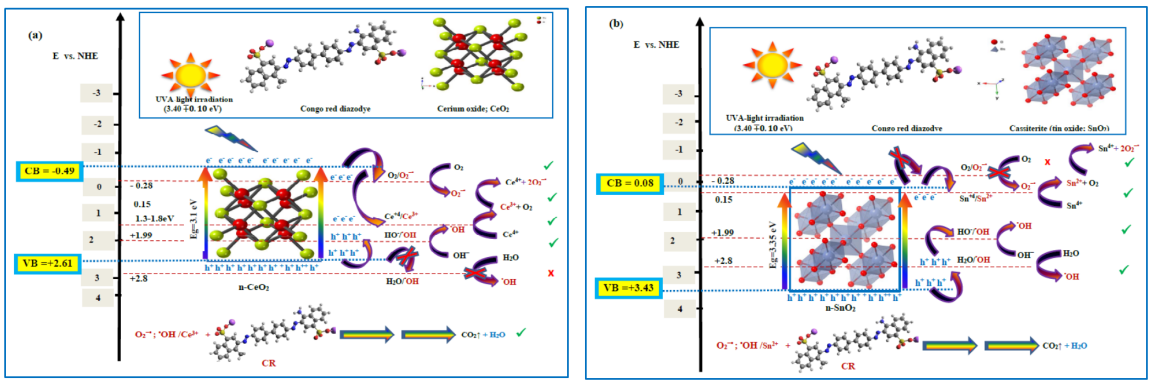

Figure 16. Mechanisms of the photodegradation of CR azodye by CeO_2-500 (a) and SnO_2-450 (b) (Figures were created using CrystalMaker software). ([nano-catalysts] =0.5 g/L, [CR]=20 mg/L, pH= 7 (for CeO_2) and 8 (for SnO_2), T =25°C), λ_{max} = 365 nm, Intensity = 90 J. cm^{-2} and irradiation time = 100 min).

$$HO^- + h^+_{(VB)} \rightarrow {}^{\bullet}OH \quad (16)$$

$$O_2^{\bullet-}/{}^{\bullet}OH + CR \rightarrow \text{Intermediates products} \rightarrow \text{Mineralized products}(H_2O \text{ and } CO_2) \quad (17)$$

For SnO_2-450 (Fig. 16b), the generated electrons in CB are not able to reduce O_2 into $O_2^{\bullet-}$, while they can provoke reduction of Sn^{4+} to Sn^{+2} species Eq. 19, since the CB edge potential of SnO_2-450 (0.08 eV) is more positive

Table 12. Photocatalytic degradation of various pollutants with the application of SnO_2 and CeO_2 as semiconductor photocatalytic materials

IC	CD ($g.L^{-1}$)	TP	PC ($mg.L^{-1}$)	Light Source	η (%) (Process Time)	Ref.
SnO_2 NPs	0.2	MB	10	portable UV sterilization lamp (3×11W)	84.78% (100 min)	[125]
G-SnO_2 NPs	2.7	MB RhB	100 100	Visible light lamp	96.35% 91.26% (80 min)	[126]
SnO_2 nanostructures	2.5	MO	10	500 W ultraviolet lamps	61.86% (240 min)	[127]
SnO_2 NPs	0.2 1	MO	10 10	Sunlight 9 W LED light	99 (6 min) 97(25 min)	[128]
Biosynthesis of tin oxide (SnO_2) NPs	0.54	MB EBT	100	Sunlight	90% 83% (300 min)	[129]
SnO_2 NPs	-	MB	-	UVA- light fluorescent light	82 % 80 % (70 min)	[130]
SnO_2 NPs	2.5×10^{-6} M	MB CR EY	2.7×10^{-6} M 2.7×10^{-6} M 2.7×10^{-6} M	UV light source (254 nm)	40% (20 min) 100% (12 min) 100% (18 min)	[131]
C. spinosa mediated synthesized SnO_2 NPs	250	CR	10^{-4} M	Heber Multilamp Photoreactor (365 nm)	92% (50 min)	[132]
Hierarchical SnO_2 Microflowers	1	RhB	10	UV light (300W mercury lamp)	99% (120 min)	[133]
CeO_2 Nanowires	0.2	MO	0.01 mM	250W Hg lamp	Nanowires (8%) Nanorods (78%) (100 min)	[134]
CeO_2 Nanostructure	1.0	XMY6G	10	125 Hg lamp (365 nm)	100% (30 min)	[135]
CeO_2 NPs	1.3	Ph 2-CP 2-BP 2-NP	50	Sunlight, 900 x 10^2 lx	Ph (<35%) 2-CP (∼98%) 2-BP (∼96%) 2-NP (99%) (180 min) TOC Ph(∼20%) 2-CP(∼94%) 2-BP(91%) 2-NP(96%) (180 min)	[136]
CeO_2 X-architecture particles	1	MB	40	500W Hg lamp	98% (120 h)	[137]
CeO_2 NPs	0.6	IC MB	30	15 W (Lumek) as a UV-C source	90% (180 min)	[138]
Commercial CeO_2	1	MO	8	UV-A polychromatic irradiation (18 W with maximal emission at 365 nm) and illumination intensity of 0.66 mW/cm^2)	87 % (120 min)	[139]
biosynthesized CeO_2 NPs	0.05	MB	10	UV radiation from a 12 W UV lamp	>90% (180 min)	[140]
CeO_2 NPs	1.5	RG19 RO84 RV1 RY 81	10	Solar light, 990 × 100 lx	RG19 (>95%) RO84 (>95%) RV1 (>99.9%) RY 81(>95%) (240 min)	[141]
CeO_2 NPs	0.3	RhB	10^{-5} mol. L^{-1}	6 lamps (254 nm, PHILIPS TL-D, 15 W, ∼9.55 mW/cm^2)	Rod (3.7%) Bean (11.27%) Hexagon (20.63%) Rod/Cube (9.94%) (60 min)	[142]
SnO_2 NPs CeO_2 NPs	0.5	CR	20	6 W ultraviolet (365 nm, BLX-E365) photoreactor	CeO_2 NPs (76.44%) SnO_2 NPs (61.63 %) (100 min)	This work

IC: Identification catalyst; TP: Target Pollutant, CD: Catalyst dose, PC: Pollutant concentration, η (%) :Degradation Eciency, Ref.: Reference, NPs: Nanoparticles, RhB: Rhodamine B ; MB :Methylene blue ; G-SnO_2 NPs: Green synthesis of tin-oxide nanoparticles, eriochrome black-T (EBT), CR: Congo red; EY: Eosin Y. IC :indigo carmine, RG19: Reactive Green 19, RO84: Reactive Orange 84, RV1:Reactive violet 1, RY 81: Reactive Yellow 81, Ph: Phenol, 2-CP: 2-chlorophenol, 2-BP: 2-bromophenol, 2-NP: 2-nitrophenol, XMY6G: Xylene Milling Yellow 6G

than that of $O_2/O_2^{\bullet-}$ (-0.28 eV) and too negative than that of Sn^{+4}/Sn^{2+} (0.15 eV), respectively, as displayed in Table 9. The reduced Sn^{2+} subsequently reacts with O_2 to produce $O_2^{\bullet-}$ Eq. 20 Temporarily since the VB edge potential of SnO_2-450 (3.43 eV) is more positive than these of $OH^-/^{\bullet}OH$ (+1.99 eV) and $H_2O/^{\bullet}OH$ (+2.8 eV), the photoinduced holes (h^+) in the VB which is standard potentials enter in an oxidation process with ^-OH Eq. 21 and H_2O Eq. 22 to generate $^{\bullet}OH$ radicals. The ROS species ($^{\bullet}OHs$ and $O_2^{\bullet-}$) play a crucial task in photodegrading recalcitrant CR azodye to the intermediate products and ultimately mineralized H_2O and CO_2 Eq. 23. The overall possible photocatalytic pathways may be illustrated as follows Eqs. 18-23 [143]:

$$SnO_2 + h\nu_{(\text{UVA-light})} \rightarrow \text{n-}SnO_2\{e^-_{(CB)} + h^+_{(VB)}\} \quad (18)$$

$$Sn^{4+} + e^-_{(CB)} \rightarrow Sn^{2+} \quad (19)$$

$$Sn^{2+} + 2O_2 \rightarrow 2O_2^{\bullet-} + Sn^{4+} \quad (20)$$

$$HO^- + h^+_{(VB)} \rightarrow^{\bullet} OH \quad (21)$$

$$H_2O + h^+_{(BV)} \rightarrow^{\bullet} OH \quad (22)$$

$$(O_2^{\bullet-}, ^{\bullet}OH) + \text{CR dye} \rightarrow \text{Intermediates products} \rightarrow \text{Mineralized products}(H_2O \text{ and } CO_2) \quad (23)$$

On the base of the obtained findings, the photocatalytic achievement of CeO_2-500 and SnO_2-450 catalysts could be ascribed to ROS species ($^{\bullet}OH$ and $O_2^{\bullet}-$) as the powerful oxidizing agents involved in the redox process. Further progress in the photocatalytic response was accredited to the oxygen vacancies (Ce^{3+} and Sn^{2+} ions) as dynamic centers for water splitting [144], which facilitates photo-excited electron-hole separation, prevents rapid recombination of the electron-hole pairs and results in an increase in the photocatalytic efficiency of CeO_2-500 as well as SnO_2-450 [145, 146].

3.16 Comparison of various cerium- and stannium based photocatalysts' performance

The comparison of various CeO_2 - and SnO_2-based photocatalysts' performance for degradation of synthesized dyes was established. Examples of SnO_2 and CeO_2 applications as single photocatalysts in pollutant degradation are presented in Table 12. While Compared to other literature, as displayed in Table 12, this current report we are among the first research group to report on CeO_2 and SnO_2 NPs shows the highest photodegradation percentage of diazo dye (Congo red) by using Ethylene Glycol ($C_2H_6O_2$) and Oxalic Acid Dihydrate ($H_2C_2O_4$) as chelating and reducing agents and also it was one of the simplest and promising technique providing an outstanding optical, electrical, and magnetic properties semiconducting nanoparticles for eradication of organic and inorganic pollutants.

4. Conclusion

CeO_2 and SnO_2 were successfully synthesized via coprecipitation methods. These nanoscale materials demonstrated auspicious structural morphological and optical performaces. XRD peak profile analysis was undertaken to assess microstructure parameters via various mathematical models. Cubic and tetragonal structures of CeO_2 of SnO_2 were evidenced by XRD analysis, respectively. Meanwhile, spherical shapes with a strong agglomeration of CeO_2-500 NPs and a foamed body of SnO_2-450 were corroborated by SEM observation. Moreover, according to the UV-Vis DRS study, the E_g values of CeO_2-500 and SnO_2-450 are 3.1 and 3.35 eV, respectively. As per the comparison of D_{XRD} values in every single model, all methods provide crystallite sizes within $10-12$ nm for CeO_2-500 and $20-30$ nm for SnO_2-450. Additionally, SM, SEAM, and MSM methods resulted in more acceptable crystallite size values; however, they were less accurate by ignoring the involvement of the microstrain. On the contrary, SSM is not realistic at all due to the negative value obtained for R^2 (-0.438 and -3.972 for CeO_2-500 and SnO_2-450, respectively) and the high-dispersed data. We could observe, for CeO_2-500, that the UDEDM method exhibited the smallest values of crystallite size (11.00 nm), intrinsic strain (0.000225), and R^2 (0.9325), implying that intrinsic strain was anisotropic in nature. Meanwhile, in the case of SnO_2-450, all the models result in almost similar microstructure properties, while R^2 is small for UDM (0.345), USDM (0.345), and UDEDM (0.4535), an indication of the high dispersion of experimental data. It is obvious that all the models are not realistic. Nevertheless, SSPM gave the highest values of intrinsic strain and R^2 (0.9975), which would suggest that lattice strain was isotropic in the environment. In comparison with the previous analyzed models, HWM model gave the highest of R^2 (0.9031) and exhibited a decrease in the intrinsic strain. Both explored materials exhibited promising photocayatlytic performance as a result of 76.44% and 61.63% CR degradation for CeO_2-500 and SnO_2-450, respectively. Kinetic data better fittrd with pseudo-first order model. Consequently, the outstanding degradation of CR could be can be synergistically explained by the involvement of ROS ($^{\bullet}OH$ and $O_2^{\bullet-}$), as the robust oxidizing agents implicated in the redox process, and Ce^{4+}/Ce^{3+} and Sn^{4+}/Sn^{4+} redox systems together with oxygen vacancy (large intrinsic crystal defects; Ce^{4+}-O and Sn^{4+}-O defects sites), as primary driving forces ultimately facilitate charge separation of carriers, reduce their recombination rate and thus boost their photocayatlytic effectiveness.

Acknowledgments

The author acknowledges the support from the Directorate-General for Scientific Research and Technological Development. (DGSRTD), the Ministry of Higher Education and Scientific Research (Algeria) and the University of Science and Technology of Oran Mohamed Boudiaf, Algeria.

Authors Contributions
All authors have contributed equally to prepare the paper.

Availability of Data and Materials
Data will be made available on request.

Conflict of Interests
The authors declare that they have no known competing financial interests or personal relationships that could have appeared to influence the work reported in this paper.

References

[1] A. Verma, S.P. Gautam, K.K. Bansal, Prabhakar N, and J. M. Rosenholm. *Medicines*, **6**(2019)(1):39, . DOI: https://doi.org/10.3390/medicines 6010039.

[2] P.G. Jeelani, P. Mulay, R. Venkat, and C. Ramalingam. *Silicon*, **12**(2020):1337–1354. DOI: https://doi.org/10.1007/s12633-019-00229-y.

[3] M.T. Yashima, S. Sasaki, Y. Yamaguchi, M. Kakihana, M. Yoshimura, and T. Mori. *Appl. Phys. Lett.*, **72**(1998):182–184. DOI: https://doi.org/10.1063/1.120678.

[4] K. Nikolaou. *Sci. Total Environ.*, **235**(1999):71–76. DOI: https://doi.org/10.1016/S0048-9697(99)00191-6.

[5] X. Feng, D.C. Sayle, Z.L. Wang, M.S. Paras, B. Santora, A.C. Sutorik, T.X.T. Sayle, Y.Yang, Y. Ding, X. Wang, and Y.S.Her. *Science*, **103**(2003):1504–1508, . DOI: https://doi.org/10.1126/science.1125767.

[6] I. Nobuhito, M. Toshiyuki, H. Hidekazu, and A. Ginya. *Chem. Mater.*, **15**(2003):2289–2291. DOI: https://doi.org/10.2320/matertrans.M2016285.

[7] J. Zhou and D. R. Mullins. *Surf. Sci.*, **600**(2006):1540–1546. DOI: https://doi.org/10.1016/j.susc.2006.02.009.

[8] N. Kakuta, N. Morishima, M. Kotobuki, T. Iwase, T. Mizushima, Y. Sato, and S. Matsuura. *Appl. Surf. Sci.*, **121/122**(1997):408–412. DOI: https://doi.org/10.33945/SAMI/JCR.2019.1.99113.

[9] M. Lira-Cantu and F. C. Krebs. *Sol. Energy Mater. Sol. Cells*, **90**(2006):2076–2086. DOI: https://doi.org/10.1016/j.solmat.2006.02.007.

[10] M. Flytzani-Stephanopoulos, M. Sakbodin, and Z. Wang. *Science*, **312**(2006):1508–1510. DOI: https://doi.org/10.1126/science.1125684.

[11] A.H. Morshed, M.E. Moussa, S.M. Bedair, R. Leonard, S.X. Liu, and N. El-Masry. *Appl. Phys. Lett.*, **70**(1997):1647–1649. DOI: https://doi.org/10.1063/1.118658.

[12] I. Celardo, J.Z. Pedersen, E. Traversa, and L. Ghibelli. *Nanoscale*, **3**(2011):1411–1420. DOI: https://doi.org/10.1039/C0NR00875C.

[13] S. Das, J.M. Dowding, K.E. Klump, J.F. McGinnis, W. Self, and S. Seal. *Nanomedicine*, **8**(2013)(9):1483–1508. DOI: https://doi.org/10.2217/nnm.13.133.

[14] C. Walkey, S. Das, S. Seal, J. Erlichmana, K. Heckman, L. Ghibelli, E. Traversa, J. F. McGinnis, and W. T. Self. *Sci. Nano.*, **2**(2015):33–53. DOI: https://doi.org/10.1039/C4EN00138A.

[15] P. Muhammed Shafi and A. Chandra Bosea. *AIP ADVANCES*, **5**(2015):057137–10. DOI: https://doi.org/10.1063/1.4921452.

[16] T.W. Kim, D.U. Lee, D.C. Choo, J.H. Kim, H.J. Kim, J.H. Jeong, M. Jung, J. H. Bahang, H.L. Park, Y.S. Yoon, and J.Y. Kim. *J. Phys. Chem. Sol.*, **63**(2002): 881–885. DOI: https://doi.org/10.1016/S0022-3697(01)00243-8.

[17] M. Marikkannan, V. Vishnukanthan, A. Vijayshankar, J. Mayandi, and J.M. Pearce. *AIP Adv.*, **5**(2015)(2): 027122. DOI: https://doi.org/10.1063/1.4909542.

[18] S. Parvathya and B.R. Venkatramanb. *J. Nanosci. Curr. Res.*, **2**(2017):2:1, . DOI: https://doi.org/10.4172/2572-0813.1000111.

[19] M.A. Andio, P.N. Browning, P.A. Morris, and S.A. Akbar. *Sensor. Actuator. B Chem.*, **165**(2012)(1):13–18. DOI: https://doi.org/10.1016/j.snb.2011.12.045.

[20] L. S. Reddy, K. Yadav, B. Manjunath, C. Archana, Madhu. H. Raja Naika, H. Nagabhushana, C. Kavitha, and G. Nagaraju. *EPJ Plus.*, **7**(2016): 131:154. DOI: https://doi.org/10.1140/epjp/i2016-16154-y.

[21] N.R. Thammadihalli, R. Thippeswamy, N. Ganganagappa, and R. Hanumanaika. *ChemistryOpen*, **4**(2015):146–154. DOI: https://doi.org/10.1002/open.201402046.

[22] F. Gao, Q. Lu, and S. Komarneni. *J. Nanosci. Nanotechnol*, **6**(2006):3812–3819. DOI: https://doi.org/10.1166/jnn.2006.609.

[23] W. Ke, G. Fang, Q. Liu, L. Xiong, P. Qin, H. Tao, J. Wang, H. Lei, B. Li, and J. Wan. *J. Am. Chem. Soc.*, **137**(2015)(21):6730–6733. DOI: https://doi.org/10.1021/jacs.5b01994.

[24] A. Verma, P. Chaudhary, R.K. Tripathi, and B.C. Yadav. *Sensor Actuator Phys.*, **321**(2021):112600, . DOI: https://doi.org/10.1016/j.sna.2021.112600.

[25] M.G. Helander, Z.B. Wang, J. Qiu, M.T. Greiner, D.P. Puzzo, Z.W. Liu, and Z.H. Lu. *Science*, **332**(2011)(6032):944–947. DOI: https://doi.org/10.1126/science.1202992.

[26] J.L. Vossen and E.S. Poliniak. *Thin Solid Films*, **13**(1972)(2):281–284. DOI: https://doi.org/10.1016/0040-6090(72)90296-9.

[27] A. Cabot, A. Dieguez, A. Romano-Rodrıguez, J.R. Morante, and N. Barsan. *Sensor. Actuator. B Chem.*, **79**(2001)(2-3):98–106. DOI: https://doi.org/10.1016/S0925-4005(01)00854-1.

[28] C. Liewhiran, N. Tamaekong, A. Wisitsoraat, and S. Phanichphant. *Sensor Actuator. B Chem.*, **163**(2012)(1):51–60. DOI: https://doi.org/10.1016/j.snb.2011.12.097.

[29] A. Kolmakov, D.O. Klenov, Y. Lilach, S. Stemmer, and M. Moskovits. *Nano Lett.*, **5**(2005)(4):667–673. DOI: https://doi.org/10.1021/nl050082v.

[30] R.K. Rawat, A. Singh, and P. Chauhan. *ECS J. Solid State Sci. Technol.*, **10**(2021)(9):097001. DOI: https://doi.org/10.1149/2162-8777/ac2324.

[31] X. Wang, X. Zhou, K. Yao, J. Zhang, and Z. Liu. *Carbon*, **49**(2011)(1):133–139, . DOI: https://doi.org/10.1016/j.carbon.2010.08.052.

[32] S. Mishra, S. Soren, A.K. Debnath, D.K. Aswal, N. Das, and P. Parhi. *Optik - International J. for Light and Electron Optics*, **169**(2018):125–136, . DOI: https://doi.org/10.1016/j.ijleo.2018.05.045.

[33] N. Ozer. *Sol Energy Mater. Sol. Cells.*, **68**(2001): 391–400, . DOI: https://doi.org/10.1016/S0927-0248(00)00371-8.

[34] H. Li, G. Liua, and X. Duana. *Mater. Chem. Phys.*, **115**(2009):9–13. DOI: https://doi.org/10.1016/J.MATCHEMPHYS.2009.01.014.

[35] H.I. Chen and H.Y. Chang. *Ceram. Int.*, **31**(2005)(6):795–802. DOI: https://doi.org/10.1016/j.ceramint.2004.09.006.

[36] Y. Feng, Y. Cui, J. Liu, and B.E. Logan. *J. Hazard. Mater.*, **178**(2010):29–34, . DOI: https://doi.org/10.1016/j.jhazmat.2009.12.101.

[37] S.H. Hwang, C. Kim, and J. Jang. *Catal. Commun.*, **12**(2011):1037–1041. DOI: https://doi.org/10.1016/j.catcom.2011.02.024.

[38] K.S. Lin and S. Chowdhury. *Int. J. Mol. Sci.*, **11**(2010):3226–3251. DOI: https://doi.org/10.3390/ijms11093226.

[39] Z. Wu, M. Li, J. Howe, H.M. Meyer, and S.H. Overbury. *Langmuir*, **26**(2010):16595–16606. DOI: https://doi.org/10.1021/la101723w.

[40] A Hartridge and A. K. Bhattacharya. *J. Phys. Chem. Solids.*, **63**(2002)(2):441–448. DOI: https://doi.org/10.1016/S0022-3697(01)00158-5.

[41] N. Ozer. *Sol Energy Mater. Sol. Cells.*, **68**(2001): 391–400, . DOI: https://doi.org/10.1016/S0927-0248(00)00371-8.

[42] E. Kusmierek. *Catalysts*, **10**(2020):1435. DOI: https://doi.org/10.3390/catal10121435.

[43] I. Erdem, H.H. Kart, and T. Cagin. *J. Alloys Comp.*, **633**(2015):272–279. DOI: https://doi.org/10.1016/j.jallcom.2015.01.235.

[44] V. Soni, S. P. Singh, S. Thakur, T. Ahamad, V. Nguyen, V. Chaudhary, N. Kumar, S. Kaya, C. Mustansar Hussain, and P.j. Raizada. *Journal of the Taiwan Institute of Chemical Engineers*, **159**(2024):105419. DOI: https://doi.org/10.1016/j.jtice.2024.105419.

[45] A. Yousefi and A. Nezamzadeh-Ejhieh. *Iranian J. Catal.*, **11**(2021)(3):247–259, .

[46] R. Anitha, K.V. Ramesh, and K.H. Sudheerkumar. *Int. J. Pharm. Bio. Sci. B*, **8**(2017):933–936. DOI: https://doi.org/10.22376/IJPBS.2017.8.2.B933-936.

[47] S. Parvathya and B.R. Venkatramanb. *J. Nanosci. Curr. Res.*, **2**(2017):1–9, . DOI: https://doi.org/10.4172/2572-0813.1000111.

[48] S. Mishra, S. Soren, A.K. Debnath, D.K. Aswal, N. Das, and P. Parhi. *Optik - International J. for Light and Electron Optics*, **169**(2018):125–136, . DOI: https://doi.org/10.1016/j.ijleo.2018.05.045.

[49] S.N. Matussin, F. Khan, M.H. Harunsani, Y.M. Kim, and M.M. Khan. *ACS Omega*, **8**(2023):11868–11879. DOI: https://doi.org/10.1021/acsomega.2c07058.

[50] R. Huang, C. Wu, S. Huang, D. Chen, Q. Zhang, Q. Wang, Z. Hu, Y. Jiang, B. Zhao, and Z. Chen. *Acta Crystallogr C Struct Chem.*, **5**(2019)(6):812–821. DOI: https://doi.org/10.1107/S2053229619006399.

[51] M. Hojamberdiev, B. Czech, A.C. Göktaş, K. Yubuta, and Z.C. Kadirova. *Journal of Alloys and Compounds*, **27**(2020):154339. DOI: https://doi.org/10.1016/j.jallcom.2020.154339.

[52] Z. Weldemichael Zena, L. Teshome Tufa, D. M. Andoshe, A.B. Gemta, and F. Birhanu Dejene. *Phys. Scr.*, **98**(2023)(10):105974. DOI: https://doi.org/10.1088/1402-4896/acfa44.

[53] J.V. Kumar, D. Karthika, P. Rosaiah, S. Devanesan, R. Mythili, M. Dhananjaya, and S.W. Joo. *Process Safety and Environmental Protection*, **188**(2024):398–405, . DOI: https://doi.org/10.1016/j.psep.2024.05.088.

[54] Lei Liao, Pengxiang Jia, Yingrong Jin, Fanggong Cai, and Qinyong Zhang. *Journal of Physics and Chemistry of Solids*, **188**(2024):111946. DOI: https://doi.org/10.1016/j.jpcs.2024.111946.

[55] C.S. Riccardi, R.C. Lima, M.L. dos Santos, P.R. Bueno, J.A. Varela, and E. Longo. *Sol. State Ionics*, **180**(2009):288–291. DOI: https://doi.org/0.1016/j.ssi.2008.11.016.

[56] S. Chaiwichian, B. Inceesungvorn, K. Pingmuang, K. Wetchakun, S. Phanichphant, and N. Wetchakun. *Enginnering J.*, **16**(2012):153–160. DOI: https://doi.org/10.4186/ej.2012.16.3.153.

[57] H.W. He, X.Q. Wu, W. Ren, P. Shi, X. Yao, and Z.T. Song. *Ceram. Internat*, **38**(2012):S501–S504. DOI: https://doi.org/10.1016/j.ceramint.2011.05.063.

[58] C.W. Raubach, L. Polastro, M.M. Ferrer, A. Perrin, C. Perrin, A.R. Albuquerque, P.G.C. Buzolin, J. R. Sambrano, Y.B. V. de Santana, J.A. Varela, and E. Longo. *J. Appl. Phys.*, **115**(2014):213514, . DOI: https://doi.org/10.1063/1.4880795.

[59] P. Chaudhary, D.K. Maurya, A. Pandey, A. Verma, R.K. Tripathi, S. Kumar, and B. C. Yadav. *Actuator. B Chem.*, **350**(2022):130818. DOI: https://doi.org/10.1016/j.snb.2021.130818.

[60] T. Haldar, U. Kumar, B. Yadav, and V.R.K. Kumar. *J. Alloys Compd*, **856**(2021):158157. DOI: https://doi.org/10.1016/j.jallcom.2020.158157.

[61] A. Singh, S. Sikarwar, and B.C. Yadav. *Mater, Res. Express*, **8**(2021)(4):045013. DOI: https://doi.org/10.1088/2053-1591/abf52e.

[62] R.K. Tripathi, O.S. Panwar, I. Rawal, C.K. Dixit, A. Verma, P. Chaudhary, A. K. Srivastava, and B.C. Yadav. *J. Mater. Sci. Mater. Electron.*, **32**(2021)(2): 2535–2546. DOI: https://doi.org/10.1007/s10854-020-05020-z.

[63] U. Kumar, Y.-H. Yang, Z.-Y. Deng, M.-W. Lee, W.-M. Huang, and C.-H. Wu. *Sensor. Actuator. B Chem.*, **353**(2022):131192, . DOI: https://doi.org/10.1016/j.snb.2021.131192.

[64] K. Balakrishnan and N. Murugasean. *Int. J. Nano Dimens. (IJND)*, **12**(2021)(1):76–72. DOI: https://doi.org/10.22034/ijnd.2021.677125.

[65] S. Naz, I. Javid, S. Konwar, K. Surana, P.K. Singh, M. Sahni, and B. Bhattacharya. *SN Appl. Sci.*, **2**(2020)(5):1. DOI: https://doi.org/10.1007/s42452-020-2812-2.

[66] V. Garg, H. Sharma, D. Rehani, R. Kumari, V. Kumar, M.K. Tiwari, and M. Saxena. *Journal of Nano- and Electronic Physics*, **12**(2020)(4):04004. DOI: https://doi.org/10.21272/jnep.12(4).04004.

[67] D. Nath, F. Singh, and R. Das. *Mater. Chem. Phys.*, **239**(2020):122021, . DOI: https://doi.org/10.1016/j.matchemphys.2019.122021.

[68] M. A. Islam, A. K. M. Akther Hossain, M. Z. Ahsan, M. A. A. Bally, M. Samir Ullah, S. M. Hoque, and F. A. Khan. *RSC Adv.*, **12**(2020):8502–8519. DOI: https://doi.org/10.1039/D1RA09090A.

[69] A. Sahai and N. Goswami. *Phys E : Low-Dimens. Syst. Nanostructures*, **58**(2014):130–137, . DOI: https://doi.org/10.1016/j.physe.2013.12.009.

[70] Y. Zhu, A. Bao, B. Na, G. Su, J. Wang, and J. Lang. *RSC Adv.*, **7**(2017):3586–3593. DOI: https://doi.org/10.1039/C6RA26805F.

[71] N. Knoblauch, L. Do¨rrer, P. Fielitz, M. Schmu¨ckera, and G. Borchardt. *Phys. Chem. Chem. Phys.*, **17**(2015):5849–5860. DOI: https://doi.org/10.1039/c4cp05742b.

[72] Z.T. Ichlas, R.A. Rustandi, and M.Z. Mubarok. *Journal of Cleaner Production*, **264**(2020):121675. DOI: https://doi.org/10.1016/j.jclepro.2020.121675.

[73] C.W. Raubach, L. Polastro, M.M. Ferrer, A. Perrin, C. Perrin, A.R. Albuquerque, P.G.C. Buzolin, J. R. Sambrano, Y.B. V. de Santana, J.A. Varela, and E. Longo. *J. Appl. Phys.*, **115**(2014):213514, . DOI: https://doi.org/10.1063/1.4880795.

[74] A. K. Zak, W.H. Abd, M.E. Majid, and R. A. Yousefi. *Solid State Sci.*, **13**(2011):251–256, . DOI: https://doi.org/10.1016/j.solidstatesciences.2010.11.024.

[75] A. K. Zak, W.H. Abd, M.E. Majid, and R. A. Yousefi. *Solid State Sci.*, **13**(2011):251–256, . DOI: https://doi.org/10.1016/j.solidstatesciences.2010.11.024.

[76] J.D. Rodney, S. Deepapriya, P.A. Vinosha, S. Krishnan, S. J. Priscilla, R. Daniel, and S.J. Das. *Optik*, **161**(2018):204–216, . DOI: https://doi.org/10.1016/j.ijleo.2018.01.125.

[77] M.S. Hossain, M. Mahmud, M.B. Mobarak, and S. Ahmed. *Chem. Pap.*, **76**(2022):1593–1605, . DOI: https://doi.org/10.1007/s11696-021-01949-5.

[78] E. Abdelkader, L. Nadjia, B. Naceur, and L. Favier-Teodorescu. *Cerâmica*, **68**(2022):84–96. DOI: https://doi.org/10.1590/0366-69132022683853181.

[79] A. Ayeshamariam, V. S. Vidhya, S. Sivaranjani, M. Bououdina, R. PerumalSamy, and M. Jayachandran. *Nanoelectronics and Optoelectronics*, **8**(2013): 1–8. DOI: https://doi.org/10.1166/jno.2013.1471.

[80] D. Nath, F. Singh, and R. Das. *Mater. Chem. Phys.*, **239**(2020):122021, . DOI: https://doi.org/10.1016/j.matchemphys.2019.122021.

[81] P. Bindu and S. Thomas. *J. Theor. Appl. Phys.*, **8**(2014):123–132. DOI: https://doi.org/10.1007/s40094-014-0141-9.

[82] I-T. Liu, M-H. Hon, and L. Gaik Teoh. *Mater. Transac.*, **58**(2017)(3):505–508. DOI: https://doi.org/10.2320/matertrans.M2016285.

[83] K. Balakrishnan and N. Murugesan. *Int. J. Nano Dimens*, **12**(2021)(1):76–82. URL http://creativecommons.org/licenses/by/4.0/.

[84] M. Rabiei, A. Palevicius, A. Monshi, S. Nasiri, A. Vilkauskas, and G Janusas. *Nanomaterials*, **10**(2020):1627. DOI: https://doi.org/10.3390/nano10091627.

[85] M. Bin Mobarak, M. Sahadat Hossain, F. Chowdhury, and S. Ahmed. *Arabian Journal of Chemistry*, **15**(2022):104117. DOI: https://doi.org/10.1016/j.arabjc.2022.104117.

[86] A. Monshi and P.F. Messer. *J. Mater. Sci.*, **26**(1991):3623–3627. DOI: https://doi.org/10.1007/BF00557154.

[87] M.J. Mayo. *Int. Mater. Rev.*, **41**(1996):85–115. DOI: https://doi.org/10.1179/imr.1996.41.3.85.

[88] N. Rani, S. Chahal, A.S. Chauhan, P. Kumar, R. Shukla, and S.K. Singh. *Materials Today: Proceedings*, **12**(2019):543–548, . DOI: https://doi.org/10.1016/j.matpr.2019.03.096.

[89] R. Jacob and J. Isac. *Int. J. Chem. Stud.*, **2**(2015)(5): 12–21.

[90] V.D. Mote, Y. Purushotham, and B.N. Dole. *J. Theor. Appl. Phys.*, **6**(2012). DOI: https://doi.org/10.1186/2251-7235-6-6.

[91] P. Vasudevan. *Journal of Molecular Structure*, **1272**(2023):134144. DOI: https://doi.org/10.1016/j.molstruc.2022.134144.

[92] T. Amutha, M. Rameshbabu, S. Muthupandi, and K. Prabha. *Materials Today: Proceedings*, **49**(2022):2624–2627. DOI: https://doi.org/10.1016/j.matpr.2021.08.044.

[93] M. Isik, S. Delice, and N.M. Gasanly. *Physica E*, **150**(2023):115712. DOI: https://doi.org/10.1016/j.physe.2023.115712.

[94] S. Adachi. *Springer: New York. NY. USA*, (2004). DOI: https://doi.org/10.1007/1-4020-7821-8.

[95] N. J. Tamanna, M. S. Hossain, N. M. Bahadur, and S. Ahmed. *Results in Chemistry*, **7**(2024):101313. DOI: https://doi.org/10.1016/j.rechem.2024.101313.

[96] K.A. Aly, N.M. Khalil, Y. Algamal, and Q.M.A. Saleem. *J. Alloy. Comp.*, **676**(2016):606–612. DOI: https://doi.org/10.1016/j.jallcom.2016.03.213.

[97] Y. Canchanya-Huaman, A.F. Mayta-Armas, J. Pomalaya-Velasco, Y. Bendezú-Roca, J. Andres Guerra, and J. A. Ramos-Guivar. *Nanomaterials*, **11**(2021):2311, . DOI: https://doi.org/10.3390/nano11092311.

[98] Md. Sahadat Hossain and S. Ahmed. *Results in Materials*, **20**(2023):100492. DOI: https://doi.org/10.1016/j.rinma.2023.100492.

[99] Y. Canchanya-Huaman, A. F. Mayta-Armas, J. Pomalaya-Velasco, Y. Bendezú-Roca, J. A. Guerra, and J. A. Ramos-Guivar. *Nanomaterials*, **11**(2021): 2311, . DOI: https://doi.org/10.3390/nano11092311.

[100] A. Verma, U. Kumar, P. Chaudhary, and B.C. Yadav. *Solid State Communications*, **348-349**(2022):114723, . DOI: https://doi.org/10.1016/j.ssc.2022.114723.

[101] G.K. Williamson and W.H. Hall. *Acta Metall.*, **1**(1953):22–31. DOI: https://doi.org/10.1016/0001-6160(53)90006-6.

[102] K. Arjunan and R. Ramesh Babu. *Ionics*, **29**(2023): 4797–4816. DOI: https://doi.org/10.1007/s11581-023-05160-2.

[103] M. Jarvin, S.S.R. Inbanathan, D. Rani Rosaline, A. Josephine Prabha, and S.A. Martin Britto Dhas. *Heliyon*, **8**(2022):e09653. DOI: https://doi.org/10.1016/j.heliyon.2022.e09653.

[104] Q. Yousefi and A. Nezamzadeh-Ejhieh. *Solid State Sciences*, **154**(2024):107584, . DOI: https://doi.org/10.1016/j.solidstatesciences.2024.107584.

[105] D. Balzar and H. Ledbetter. *J. Appl. Crystallogr*, **26**(1993)(1):97–103. DOI: https://doi.org/10.1107/S0021889892008987.

[106] M. Basak, L. Rahman, F. Ahmed, B. Biswas, and N. J. Sharmin. *J.Alloys Compd.*, **895**(2021):162694. DOI: https://doi.org/10.1016/j.jallcom.2021.162694.

[107] S. Rani, S. Verma, B. Sharma, and S. Kumar. *Physica B*, **661**(2023):414922, . DOI: https://doi.org/10.1016/j.physb.2023.414922.

[108] P. Simonov‘a, W. Pabst, and J. Cibulkov‘. *Ceramics International*, **47**(2021):35333–35347. DOI: https://doi.org/10.1016/j.ceramint.2021.09.076.

[109] L. Motevalizadeh, Z. Heidary, and M.E. Abrishami. *Bull Mater. Sci.*, **37**(2014):397–405. DOI: https://doi.org/10.1007/s12034-014-0676-z.

[110] N. Fifere, R. Ardeleanu, F. Doroftei, M. Dobromir, and A. Airinei. *Int. J. Mol. Sci.*, **25**(2024):681. DOI: https://doi.org/10.3390/ijms25010681.

[111] S. Sarkar and R. Das. *Lett.*, **13**(2018)(3):312–315. DOI: https://doi.org/10.1049/mnl.2017.0349.

[112] N. Boonprakob, N. Wetchakun, S. Phanichphant, D. Waxlert, P. Sherrell, A. Nattestad, J. Chen, and B. Inceesungvorn. *J. Colloid. Interf. Sci.*, **417**(2014):402–409. DOI: https://doi.org/10.1016/j.jcis.2013.11.072.

[113] S. Valencia, J.M. Marin, and G. Restrepo. *Open Mater. Sci. J.*, **4**(2010):9–14. DOI: https://doi.org/10.2174/1874088X01004010009.

[114] A.M. Abdulkarem, J. Li, A.A. Aref, L. Ren, E.M. Elssfah, H. Wang, Y. Ge, and Y. Yu. *Mater Res Bull.*, **46**(2011):1443–1450. DOI: https://doi.org/10.1016/j.materresbull.2011.05.005.

[115] K. Yang, D.F. Li, W.Q. Huang, X. Liang, G.F. Huang, and S.C. Wen. *Appl. Phys. A.*, **123**(2017):1–11. DOI: https://doi.org/10.1007/s00339-016-0700-9.

[116] S. Moeen, M. Ikram, A. Haider, J. Haider, A. Ul-Hamid, W. Nabgan, T. Shujah, M. Naz, and I. Shahzadi. *ACS Omega*, **7**(2022):46428–46439. DOI: https://doi.org/10.1021/acsomega.2c05133.

[117] M.R. Gholipour, C.T. Dhin, F. Béland, and T.O. Do. *Nanoscale*, **7**(2015):8187–8208. DOI: https://doi.org/10.1039/C4NR07224C.

[118] A. Habibi-Yangjeh and M. Shekofteh-Gohari. *Separation and Purification Technology*, **184**(2017):334–346. DOI: https://doi.org/10.1016/j.seppur.2017.05.007.

[119] J.D. Rodney, S. Deepapriya, P.A. Vinosha, S. Krishnan, S. J. Priscilla, R. Daniel, and S.J. Das. *Optik*, **161**(2018):204–216, . DOI: https://doi.org/10.1016/j.ijleo.2018.01.125.

[120] M.S. Hossain, M. Mahmud, M.B. Mobarak, and S. Ahmed. *Chem. Pap.*, **76**(2022):1593–1605, . DOI: https://doi.org/10.1007/s11696-021-01949-5.

[121] M. Farsi and A. Nezamzadeh-Ejhieh. *Surfaces and Interfaces*, **32**(2022):102148. DOI: https://doi.org/10.1016/j.surfin.2022.102148.

[122] A. Sahai and N. Goswami. *Phys. E: Low Dimens. Syst. Nanostruct*, **58**(2014):130–137, . DOI: https://doi.org/10.1016/j.physe.2013.12.009.

[123] D. Nath, F. Singh, and R. Das. *Mater. Chem. Phys.*, **239**(2020):122021, . DOI: https://doi.org/10.1016/j.matchemphys.2019.122021.

[124] K. Vasanth Kumar, K. Porkodi, and F. Rocha. *Catal. Commun.*, **9**(2008):82–84, . DOI: https://doi.org/10.1016/j.catcom.2007.05.019.

[125] E. Nurhidayah, A. Herman Yuwono, F. Septiningrum, F. Akbar Maulana, D. Dhaneswara, N. Sofyan, A. Intan Pangesty, and A. Noviyanto. *E3S Web of Conferences*, **4**(2024)(88):02016. DOI: https://doi.org/10.1051/e3sconf/202448802016.

[126] Y. Etafa Tasisa, T. Kumar Sarma, T. Kumar Sahu, and R. Krishnaraj. *Scientific Reports*, **14**(2024):10780. DOI: https://doi.org/10.1038/s41598-024-60633-2.

[127] J.Wang, H. Fana, and H. Yu. *Opt. Int. J. Light Electron Opt.*, **127**(2016):580–584. DOI: https://doi.org/10.1016/j.ijleo.2015.10.104.

[128] R. B. Rajput and R. B. Kale. *Res. Chem.*, **4**(2022):100530. DOI: https://doi.org/10.1016/j.rechem.2022.100530.

[129] M. Honarmand, M. Golmohammadi, and A. Naeimi. *Advanced Powder Technology*, **30**(2019):1551–1557. DOI: https://doi.org/10.1016/j.apt.2019.04.033.

[130] I. Buniyamin, K. Alvin Eswar, N. Asnida Asli, M. Faizal Abd Halim, Z. Khusaimi, and M.Rusop Mahmood. *Malaysia Journal of Invention and Innovation (MJII)*, **2**(2023)(3). DOI: https://doi.org/10.5281/zenodo.7800382.

[131] A. Diallo, E. Manikandan, V. Rajendran, and M. Maaza. *Journal of Alloys and Compound*, **681**(2016):561–570. DOI: https://doi.org/10.1016/j.jallcom.2016.04.200.

[132] E. Haritha, Selvaraj Mohana Roopan, G. Madhavi, G. Elango, Naif Abdullah Al-Dhabi, and Mariadhas Valan Arasu. *studies Journal of Photochemistry & Photobiology, B: Biology*, **162**(2016):441–447. DOI: https://doi.org/10.1016/j.jphotobiol.2016.07.010.

[133] J. Wang, H. Fanand, and H. Yu. *Materials Transactions*, (2015), . DOI: https://doi.org/10.2320/matertrans.M2015287.

[134] A. Phuruangrat, S. Thongtem, and T.Thongtem. *Mater. Lett.*, **196**(2017):61–63. DOI: https://doi.org/10.1016/j.matlet.2017.03.013.

[135] S. Tambat, S. Umale, and S. Sontakke. *Mater. Res. Bull.*, **76**(2016):466–472. DOI: https://doi.org/10.1016/j.materresbull.2016.01.010.

[136] M. Aslam, M.T. Qamar, M.T. Soomro, I.M.I. Ismail, N. Salah, T. Almeelbi, M.A. Gondal, and A. Hameed. *Appl. Catal. B Environ*, **180**(2016):391–402. DOI: https://doi.org/10.1016/j.apcatb.2015.06.050.

[137] X. Zheng, S. Huang, D. Yang, H. Zhai, Y. You, X. Fu, J. Yuan, X. Zhou, J. Wen, and Y. Liu. *J. Alloys Compd.*, **705**(2017):131–137. DOI: https://doi.org/10.1016/j.jallcom.2017.02.110.

[138] Á. Guzman Aponte, M. A Llano Ramírez, Y. Cadavid Mora, J. F Santa Marín, and R. Buitrago Sierra. *AIMS Materials Science*, **7**(2020)(4):468–485. DOI: https://doi.org/10.3934/matersci.2020.4.468.

[139] K. Milenova, K. Zaharieva, I. Stambolova, V. Blaskov, A. Eliyas, and L. Dimitrov. *Journal of Chemical Technology and Metallurgy*, **52**(2017)(1):13–19.

[140] G. Ramanathan, S. Vinoth Rathan, and K. R. Murali. *SN Applied Sciences*, **1**(2019):116. DOI: https://doi.org/10.1007/s42452-018-0103-y.

[141] P.K. Sane, S.Tambat, S. Sontakke, and P. Nemade. *Journal of Environmental Chemical Engineering*, **6**(2018):4476–4489. DOI: https://doi.org/10.1016/j.jece.2018.06.046.

[142] R.A. C. Amoresi, R. C. Oliveira, N. L. Marana, P. B. de Almeida, P.S. Prata, M. A. Zaghete, E. Longo, J.R. Sambrano, and A. Z. Simoes. *ACS Appl. Nano Mater*, **2**(2019):6513–6526. DOI: https://doi.org/10.1021/acsanm.9b01452.

[143] N. Laouedj, A. Elaziouti, N. Benhadria, and A. Bekka. *Journal of Rare Earths*, **36**(2018):575–587. DOI: https://doi.org/10.1016/j.jre.2018.01.004.

[144] D. Majumder, I. Chakraborty, K. Mandal, and S. Roy. *ACS Omega*, **4**(2019):4243–4251. DOI: https://doi.org/10.1021/acsomega.8b03298.

[145] Qi. Zhang, Q. Ma, J. Guo, H. Li, Y. Wang, and X. Wang. *Chemical Physics Letters*, **791**(2022):139376. DOI: https://doi.org/10.1016/j.cplett.2022.139376.

[146] Li. Kalita, K. Sonowal, P. Basyach, B. Saha, and L. Saikia. *ACS Omega*, **8**(2023):11768–11781. DOI: https://doi.org/10.1021/acsomega.2c05811.